Hydrodynamic Modeling of Pelamis® P1-750 Wave Energy Converters using WAMIT™ software

A Plan B Paper submitted in partial fulfillment of the requirements
for the degree of

Master of Science

in

Ocean and Resources Engineering

University of Hawaiʻi at Mānoa

April 2014

by

Michael Frederick

Committee:

Gérard Nihous, Chairperson
R. Cengiz Ertekin
John Wiltshire

Abstract

Large scale Wave Energy Conversion (WEC) devices using segmented hinged bodies have been proposed and tested for the past 30 years, including the Hagen-Cockerell Raft[1]. This research led the way for companies like Pelamis® to design the 3 hinged P1 WEC. The device was built, tested, and a targeted Power Matrix was published for varying wave conditions. This study intends to use the WAMIT™ software[2] to calculate the hydrodynamic motions of the hinges with a linear power take off system in order to approximate the targeted Power Matrix. In addition, the same method will be used for several devices in order to investigate how the spacing of multiple machines affects motions and power output. This may suggest optimal configurations for a large number of hinged Pelamis® P1 WECs.

Contents

List of Figures

List of Tables

Nomenclature

a	Hinge geometry coefficients (m^{-1})
A	Wave amplitude (m)
α	Wave heading (rad)
b	External torsional damping coefficient (N·m·s·rad^{-1})
B_{ij}	External damping matrix
c_g	Group velocity (m·s^{-1})
d	Water depth (m)
f	Mode Shape Function
G	Green Function
h	Heave displacement (m)
H	Wave height (m)
I	Moment of Inertia (kg·m^{2})
ω	Angular frequency (rad·s^{-1})
L	Pelamis® length (m)
m	Sectional Mass (kg·m^{-1})
M	Mass (kg)
n	Number of Pelamis® P1 devices in selected group
N	Number of Pelamis® P1 devices in field
λ	Wavelength (m)
ρ	Water density (kg·m^{-3})
P	Power (W)
$\bar{P}$	Average power (W)
Q	Power factor
s_R	Row Spacing (m)
s_C	Column Spacing (m)

S	Wave spectrum ($m^2 \cdot s \cdot rad^{-1}$)
S_b	Wetted Surface
t	Time (s)
T	Period (s)
x	X Coordinate (m)
y	Y Coordinate (m)
z	Z Coordinate (m)
θ	Hinge angle (rad)
$\dot{\theta}$	Hinge angular velocity ($rad \cdot s^{-1}$)
$\bar{\theta}$	Complex hinge angular displacement amplitude
u	Velocity ($m \cdot s^{-1}$)
V	Pelamis® submerged volume (m^3)

1. Introduction:

Wave energy converters (WEC) can be used to harvest power from the ocean on many different scales. In order for large scale WECs to make an impact on energy consumption for coastal cities, they must be deployed in large numbers. Pelamis® intends to use its WEC devices to absorb energy on a large scale with many devices deployed in the water to help power coastal cities in the North Atlantic. In order to maximize power output, multiple device interaction must be studied in order to minimize possible destructive interference and optimize area utilization.

Pelamis® P1 has 3 hinges for power absorption. Each hinge has two extra degrees of freedom (DOF), vertical motions and horizontal motions. Each hinge has 4 hydraulic pistons for energy generation, 2 for the vertical motion and 2 for the horizontal motion as shown below:

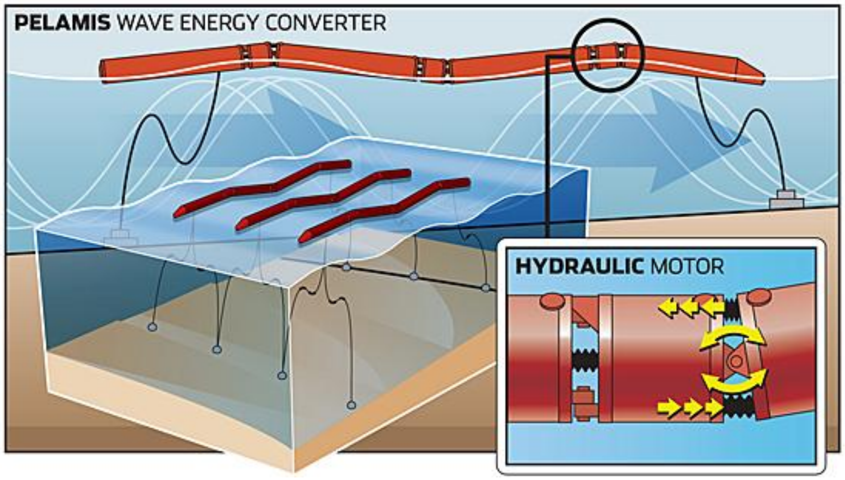

Figure 1: Pelamis® P1 Hinges[3] and Power Module

When a wave hits the hinged Pelamis® raft, the relative motion of the body sections allows for the pistons to pump a hydraulic fluid from the power module through a turbine in order to generate electricity. This power is then transported back to land through underwater cables. In this case, the cable is connected to the seabed directly from the machine. The two degrees of freedom in the hinges allow for absorption in various sea conditions. When incoming wave heights are very large, the device dives through the water due to the slack mooring at the front of the machine. There is also a shut off mechanism, when wave heights are too large. This limits the motion of the hinges to avoid stressing the machine in extreme conditions.

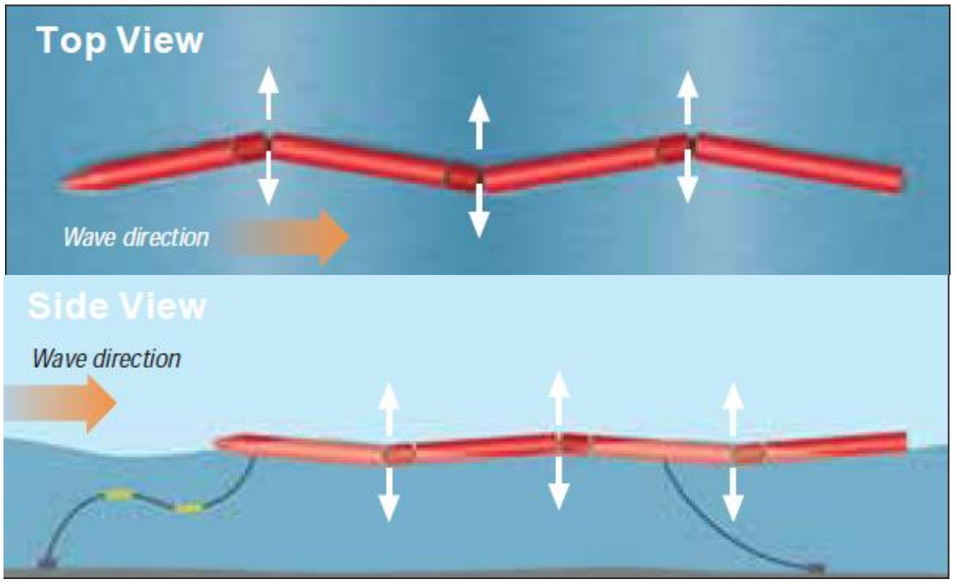

Figure 2: Pelamis® P1 Hinge Motion[3]

Shown in the figure above are the two degrees of freedom in each hinge. These allow the machine to absorb power in oblique seas, when wave energy is coming from more than one direction.

2. Objectives and Approach

The main objective of this project is to approximate the published Pelamis® Power Matrix or the 'targeted' power matrix[3], as shown below:

	Power period (T_{pow}, s)																
Significant wave height (H_{sig}, m)	5.0	5.5	6.0	6.5	7.0	7.5	8.0	8.5	9.0	9.5	10.0	10.5	11.0	11.5	12.0	12.5	13.0
0.5	idle	idle	idle	idle	idle	idle	idle	idle	idle	idle	idle	idle	idle	idle	idle	idle	idle
1.0	idle	22	29	34	37	38	38	37	35	32	29	26	23	21	idle	idle	idle
1.5	32	50	65	76	83	86	86	83	78	72	65	59	53	47	42	37	33
2.0	57	88	115	136	148	153	152	147	138	127	116	104	93	83	74	66	59
2.5	89	138	180	212	231	238	238	230	216	199	181	163	146	130	116	103	92
3.0	129	198	260	305	332	340	332	315	292	266	240	219	210	188	167	149	132
3.5	-	270	354	415	438	440	424	404	377	362	326	292	260	230	215	202	180
4.0	-	-	462	502	540	546	530	499	475	429	384	366	339	301	267	237	213
4.5	-	-	544	635	642	648	628	590	562	528	473	432	382	356	338	300	266
5.0	-	-	-	739	726	731	707	687	670	607	557	521	472	417	369	348	328
5.5	-	-	-	750	750	750	750	750	737	667	658	586	530	496	446	395	355
6.0	-	-	-	-	750	750	750	750	750	750	711	633	619	558	512	470	415
6.5	-	-	-	-	750	750	750	750	750	750	750	743	658	621	579	512	481
7.0	-	-	-	-	-	750	750	750	750	750	750	750	750	676	613	584	525
7.5	-	-	-	-	-	-	750	750	750	750	750	750	750	750	686	622	593
8.0	-	-	-	-	-	-	-	750	750	750	750	750	750	750	750	690	625

Figure 3: Published Pelamis® Power Matrix[3]

This matrix gives the 'targeted' power output of one machine for the given conditions. The given sea states are described with Significant wave height (H_s) and Power period or Energy period (T_{pow} or T_e). Shown in red are the higher power production conditions, which occur with large significant wave heights. The red zone also shows the saturation area or cutoff power production. This cap in power production represents limitations of the electrical generator. Specifics are not released by Pelamis®. Along with this, it can be assumed at conditions outside of the Matrix that the machine is shut off or unable to produce power. This matrix is recreated by looking at the response amplitude operators (RAOs) of the hinges with an estimated damping value for power take off (PTO) at each hinge.

There will be losses that need to be assumed. The hydrodynamic power output will be calculated, but in order to approximate the targeted power matrix, mechanical and electrical losses need to be estimated. The hydrodynamic power output is calculated using WAMIT™ software[2] with the body mesh being input from Rhinoceros 5 modeling software[4.] The dimensions of the hinged body are shown in Figure 4, which displays the middle line plane. The still water level is set at z=0, with the z-axis pointing vertically upwards and waves propagating from the left along the x-axis.

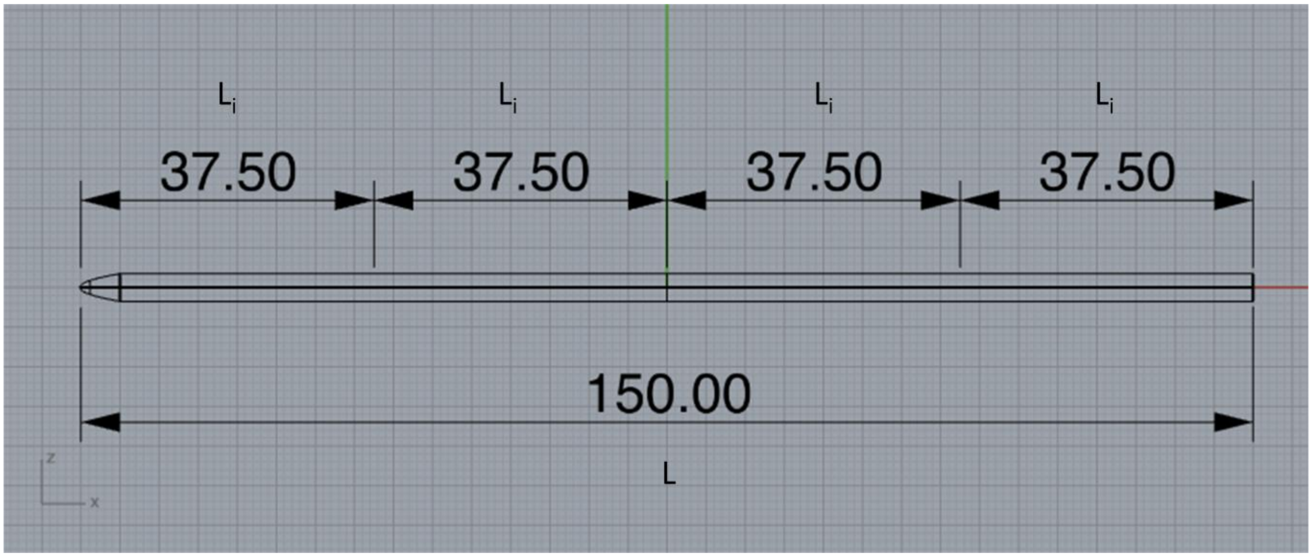

Figure 4: Pelamis® P1 Middle Line Plane

Each segment in the Pelamis® P1 has the same length, L_i, with a total length of L. The front of the machine has a paraboloidal nose cone and a cylindrical body with a diameter of 3.5m. The exact shape of the nose cone is not explicitly given in the Pelamis® P1 brochure[3] so estimates are made to recreate the shape. In doing this, the power module as seen in Figure 1, is grouped together with the rest of the cylindrical body and the hinge locations are at the center of the power modules. An overview of the entire mesh shape is shown in Figure 5.

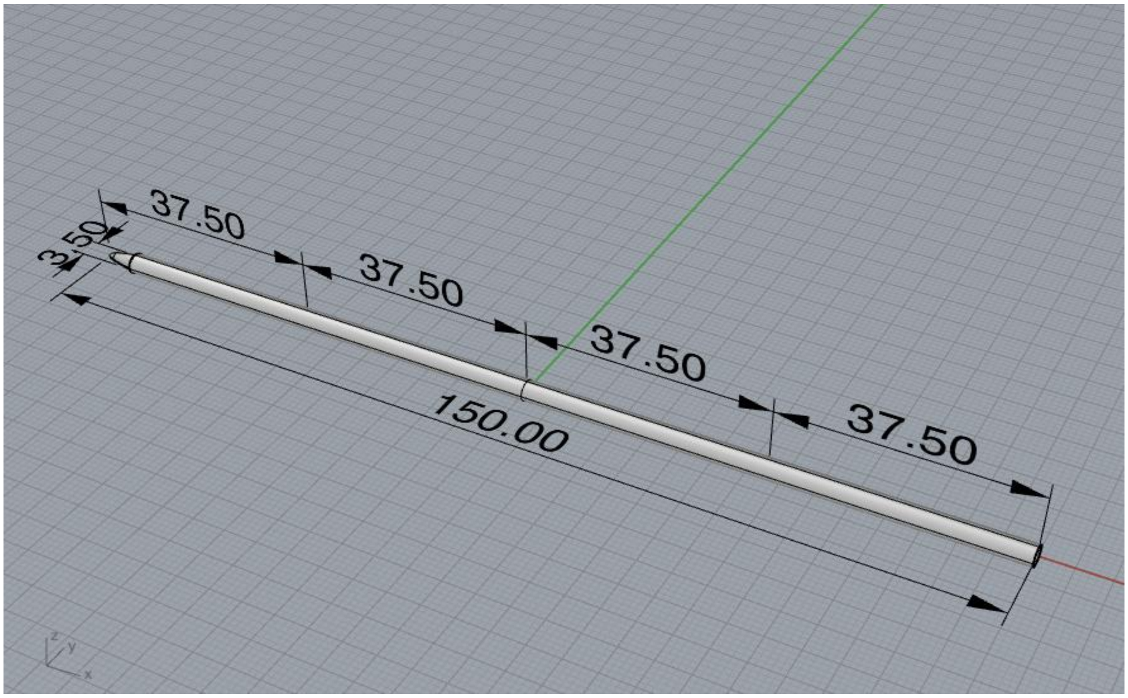

Figure 5: Pelamis® P1 Overhead view

The next goal of the project is to model multiple devices in various configurations and create power matrices for each individual machine at its location in the particular set up. Thus, constructive and destructive interactions of the bodies can be seen and a realistic power output for a field of machines can be estimated. The basic set-up is based on the Pelamis® brochure's[3] recommendation of a checkerboard pattern.

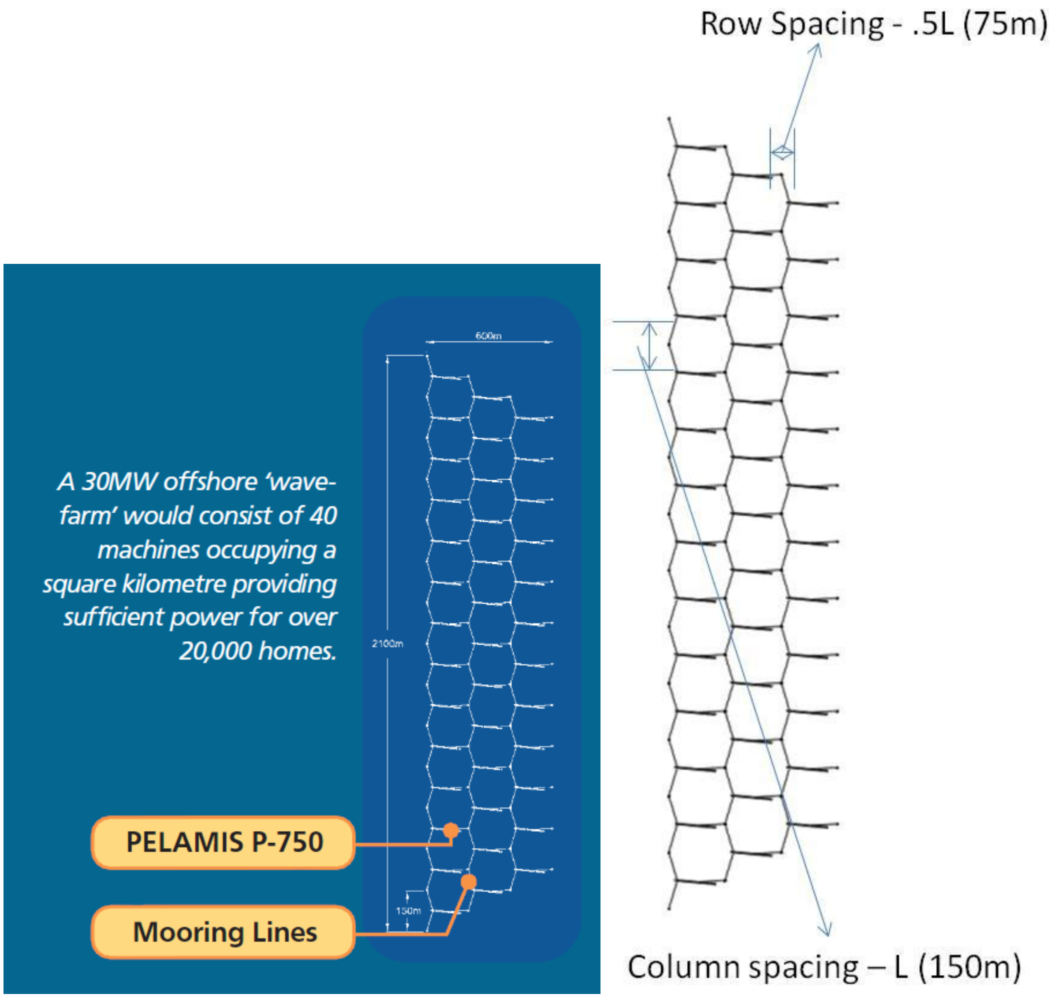

Figure 6: Left - Multiple Pelamis® P1 machine set up[3] (checkerboard pattern) Right - Column and row spacing.

Shown in Figure 6 is the suggested multiple machine set up with the two spacing variables. These column and row spacings will be varied in an effort to find the most productive set up while not taking up too large of an area. In order to model a large number of machines with the WAMIT™ software, the mesh sizes and body numbers need to be closely monitored in order to understand run times and efficiency. The WAMIT™ software will be run on a 64-bit Windows PC with 4 central processing units (CPUs) and 8GB of Random Access Memory (RAM). This will allow for a large system of equations to be solved, or in other words, high mesh resolution and large body number.

3. Equations of motion

There are two main options for creating equations of motion for a hinged body:

1. Modeling each segment as an individual body with interaction forces and motions in order to solve for the hinge motion. This will give a system of equations for each segment.

2. Develop equations for one body with additional modes or degrees of freedom for the hinge motions. This will give a system of equations for one body with additional modes for the hinges.

The second method is selected for simplicity, as it only requires a set of equations for one body. The extra hinge motions are easily input into WAMIT™ as extra modes to the system. The body is assumed to have its center of mass and gravity at the origin of the body coordinates along with the following assumptions:

1. Linear Theory
    a. Motion amplitudes are small
    b. Motions are harmonic
2. Ideal Fluid
    a. Inviscid
    b. Incompressible
3. Flow is Irrotational
4. WEC is freely floating (Slack Mooring)
5. Located in deep water, $d > \lambda/2$
6. Only vertical relative motions are modeled
7. Head Seas

For a single machine, the body coordinate origin is the same as the origin for the global coordinate system. The 6 standard rigid-body degrees of freedom and mode numbers are shown in Figure 7.

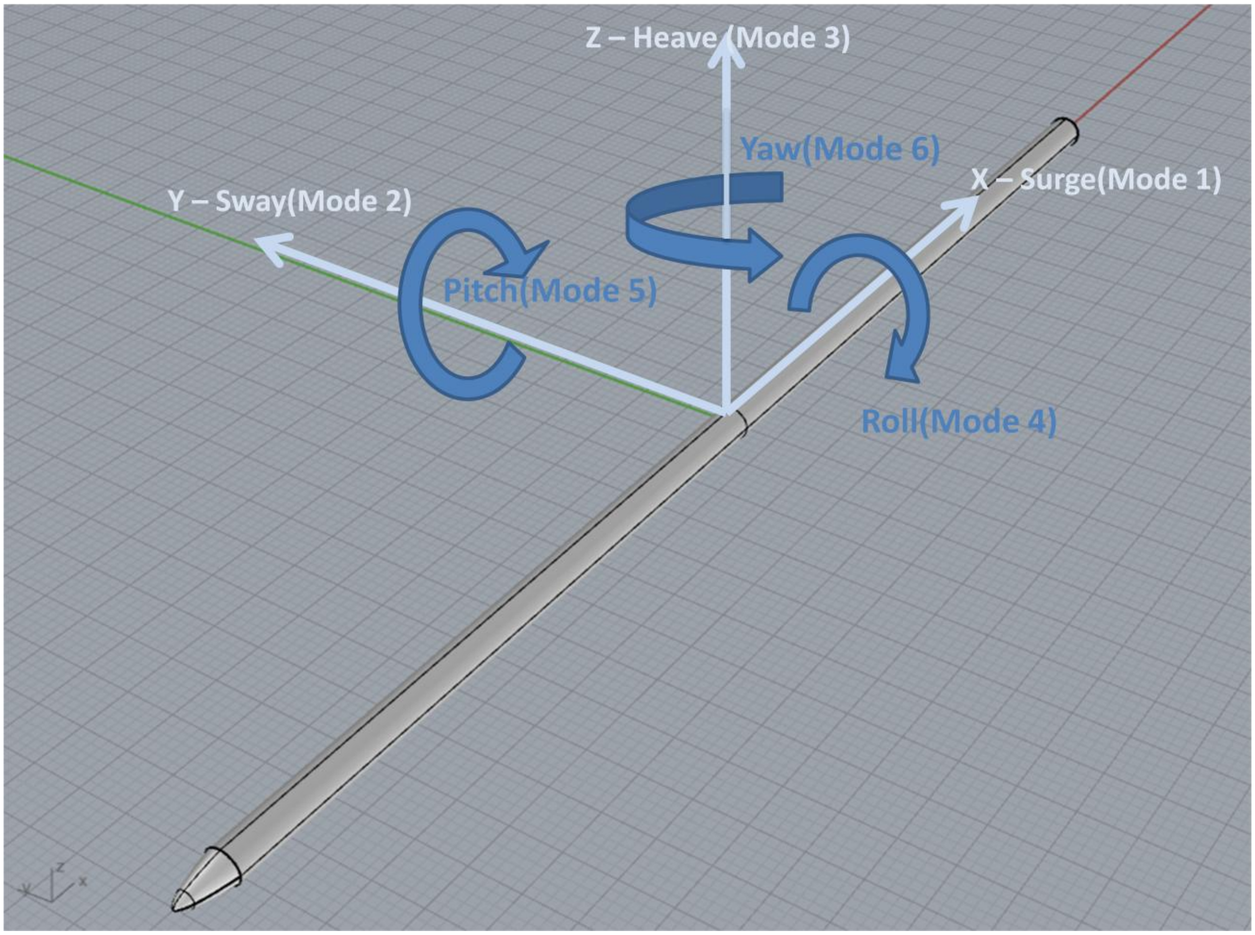

Figure 7: 6 standard rigid body degrees of freedom

The additional hinge modes are modeled as 'tent' functions5 as shown below:

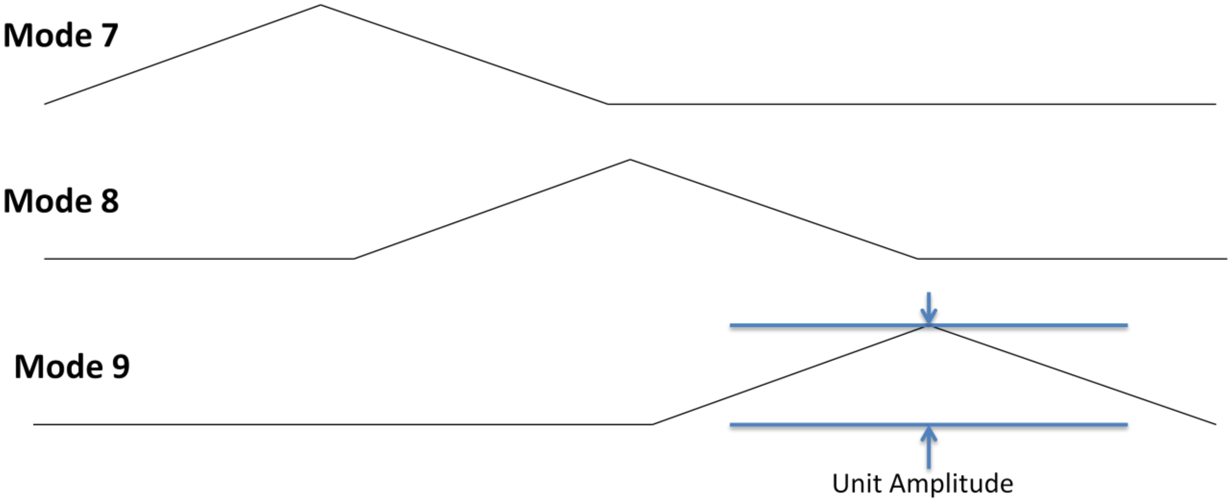

Figure 8: Additional Tent Modes for Vertical Hinge Motions

The velocity vector can be derived as the gradient of a scalar potential because the flow is assumed irrotational:

$$\vec{u} = \vec{\nabla}\Phi(x,y,z,t) \qquad \vec{\nabla} \text{ - Nabla operator} \tag{3.1}$$

Fluid incompressibility and mass conservation result in a divergence free velocity field:

$$\vec{\nabla} \bullet \vec{u} = 0 \tag{3.2}$$

Equations for irrotational flow and fluid incompressibility lead to:

$$\Delta\Phi = 0 = \frac{\partial^2\Phi}{\partial x^2} + \frac{\partial^2\Phi}{\partial y^2} + \frac{\partial^2\Phi}{\partial z^2} \tag{3.3}$$

Total Potential:

$$\Phi = \mathrm{R}(\varphi e^{i\omega t}) \text{: Where } \mathrm{R}(\,) \text{ represents the real value} \tag{3.4}$$

Scattering Potential:

$$\Phi_S = \mathrm{R}(\varphi_S e^{i\omega t}) \tag{3.5}$$

Incoming Potential:

$$\Phi_O = \mathrm{R}(\varphi_O e^{i\omega t}) \tag{3.6}$$

Complex Diffraction Potential:

$$\varphi_D = \varphi_S + \varphi_O \tag{3.7}$$

Radiation Potential:

$$\Phi_R = \mathrm{R}(\varphi_R e^{i\omega t}) \tag{3.8}$$

Complex Total Potential:

$$\varphi = \varphi_D + \varphi_R \tag{3.9}$$

Complex Incident Potential:

$$\varphi_O = (\frac{igA}{\omega})e^{-ikx\cos\alpha - iky\sin\alpha} \tag{3.10}$$

Complex Radiation potential:

$\varphi_R = \sum_{j=1}^{9} \xi_j \varphi_j$: For each degree of freedom j, ξ_j is the complex amplitude, φ_j is the corresponding unit amplitude potential (3.11)

Boundary Conditions:

Water surface:

$$\varphi_z - \frac{\omega^2}{g}\varphi = 0 \quad \text{at} \quad z=0 \tag{3.12}$$

Sea Floor:

$$\frac{\partial\varphi}{\partial z} = 0 \text{ at } z=-d \tag{3.13}$$

Body:

$$\frac{\partial\varphi_j}{\partial n} \quad ; \quad \frac{\partial\varphi_s}{dn} = -\frac{\partial\varphi_0}{dn} \text{ on } S_b \tag{3.14}$$

WAMIT™ derives integral equations by solving the radiation and diffraction potentials on the raft boundaries using Green's Theorem[12]. The integrations are approximated using discretization quadrilateral panels on the surface of the body. The method is determined as the “Low Order” method in WAMIT™, which represents the body with flat quadrilateral panels. The following equations are taken from the WAMIT™ manual[5].

Radiation velocity potential φ_j integral on body boundary:

$$2\pi\varphi_j(x) + \iint_{S_b} \varphi_j(\xi)\frac{\partial G(\xi:x)}{\partial\eta_\xi}d\xi = \iint_{S_b} n_j G(\xi:x)d\xi \tag{3.15}$$

Corresponding radiation velocity potential discretization summation equation

$$2\pi\varphi_j(x_i) + \sum_{k=1}^{N} D_{ik}\varphi_k = \sum_{k=1}^{N} S_{ik}(\frac{\partial\varphi}{\partial n})_k \tag{3.16}$$

Diffraction velocity potential φ_D integral on the body boundary

$$2\pi\varphi_D(x) + \iint_{S_b} \varphi_D(\xi)\frac{\partial G(\xi;x)}{\partial n_\xi}d\xi = 4\pi\varphi_0(x) \tag{3.17}$$

Corresponding diffraction velocity potential discretization summation equation for Low-Order Method

$$2\pi\varphi(x_i) + \sum_{k=1}^{N} D_{ik}\varphi_k = 4\pi\varphi_0(x_i) \tag{3.18}$$

Matrices D_{ik} and S_{ik} are defined by:

$$D_{ik} = \iint_{S_k} \frac{\partial G(\xi, x_i)}{\partial\eta_\xi}d\xi \tag{3.19}$$

$$S_{ik} = \iint_{s_k} G(\xi, x_i) d\xi \tag{3.20}$$

where s_k is the surface of the k-th panel.

Complex amplitudes of body motion are calculated using a 9x9 linear system

$$X_i = \sum_{j=1}^{9} [-\omega^2 (M_{ij} + M_{ij}^E + A_{ij}) + i\omega (B_{ij} + B_{ij}^E) + (C_{ij} + C_{ij}^E)]\xi_j \tag{3.21}$$

$M_{ij} + M_{ij}^E$: Mass and external matrix

A_{ij}: Added Mass

$B_{ij} + B_{ij}^E$: Hydrodynamic damping and external damping (Power Take off) matrix

$C_{ij} + C_{ij}^E$: Hydrostatic restoring coefficients and external spring matrix (Could be used as a linear anchoring system)

A_{ij}, B_{ij}, C_{ij}: Calculated by WAMIT™ based on mesh input.

4. Input Files

The WAMIT™ flow chart is shown in Figure 9. This depicts the subprograms POTEN and FORCE with their associated input and output files. The three primary input files are shown in the prescribed optional file FNAMES.WAM. These include the GDF, POT and FRC files.

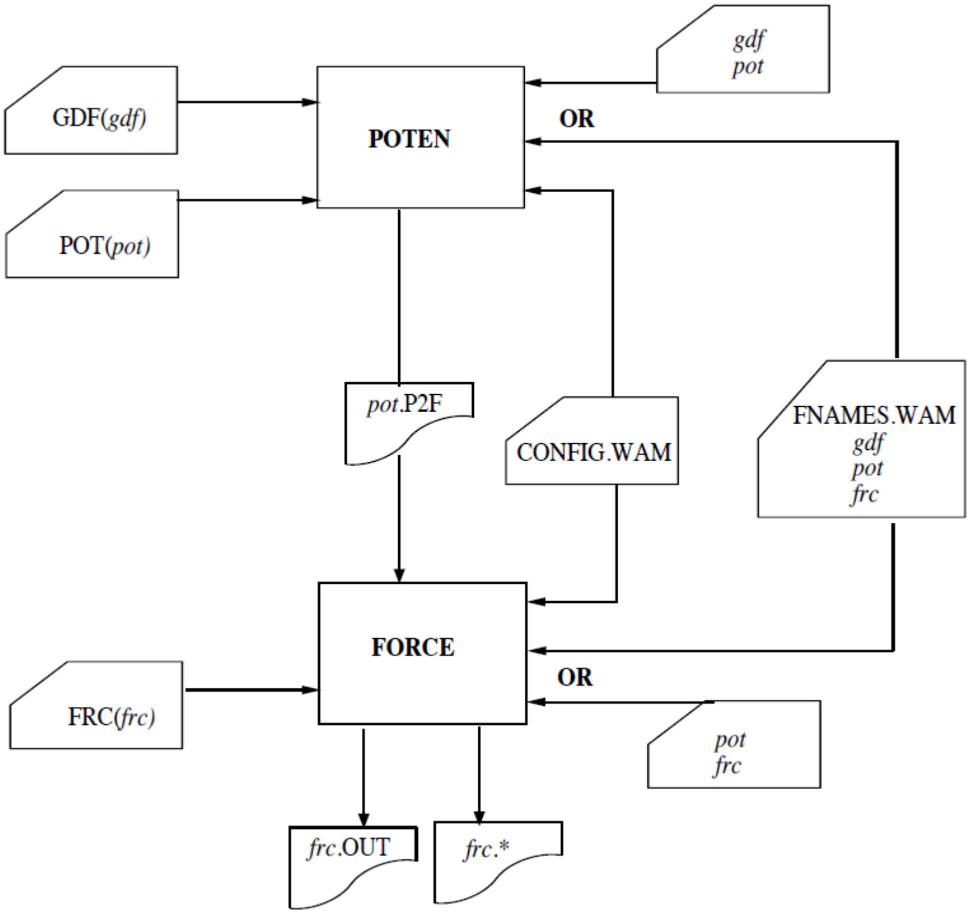

Figure 9: WAMIT™ Flow Chart[5]

The first step in the process is solving for the POTEN subprogram. This takes input from the GDF and POT files and solves for the velocity potential on the body surface and optionally also for the source strength, as described in the methodology of the previous section. After the POTEN subprogram has run, a .P2F file is created and transfers data to the new subprogram FORCE, along with the POT and FRC inputs. This FORCE subprogram evaluates physical parameters including the force and motion coefficients, as well as field data including fluid pressure, velocity and free-surface elevation[5].

The following is an overview of the input files along with the methodology used for the input files in this study:

POT:

The potential file specifies input wave conditions, water depth and body position. This includes wave headings and periods, with easy methods to specify each. The periods input in this study are 1-20s with .5s intervals at a direct heading. Upon post processing, regular (sinusoidal) wave results will be combined assuming various incident Bretschneider spectra.

GDF:

The GDF file contains information about the mesh used for the shape analyzed. This includes either a series of mesh points or a reference to already defined shapes. Along with this, symmetry, scale and gravity can be specified. The size of the mesh plays a large role in the run time of the code because it directly affects the number of equations to be solved. Symmetry is not used because of the number of hinges. For this study, three different size meshes are generated, low density (coarse), mid density (mid) and high density (fine). The coarse mesh has 850 panels, mid mesh has 5215 and the fine mesh has 14503 panels. The mid and fine meshes will be used to confirm body motions predicted with coarse mesh. For the multiple machine runs, the coarse mesh will be used in an effort to cut down computing time. Shown in Figure 10: Fine Mesh is the Fine Mesh near the nose cone. Such a fine mesh is only used for verification purposes. Also to note, only the portion of the body below the water surface, S_b, needs to be modeled, as in the potential formulation.

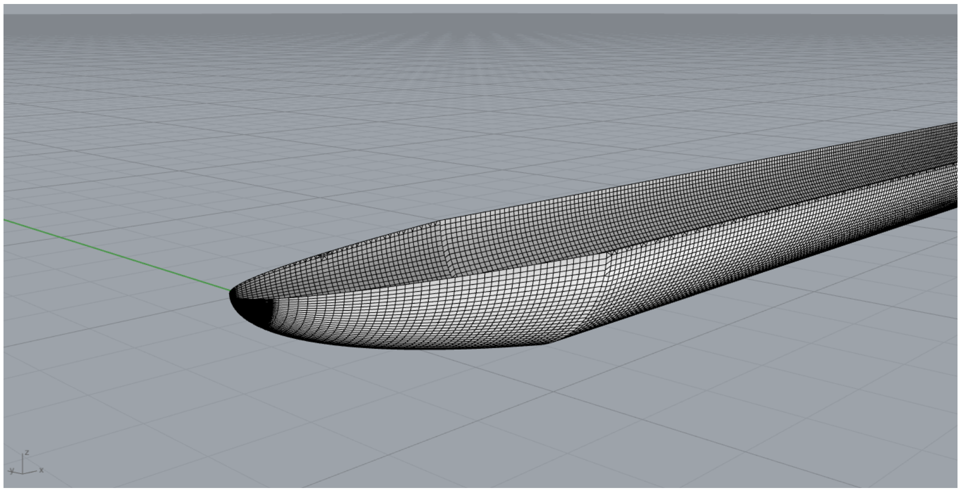

Figure 10: Fine Mesh

FRC:

The force control file contains many of the technical specifics for the body inputs and outputs. This includes the mass and inertia matrix, external damping matrix, external stiffness matrix, output specifics and optional field points to be output. For this study, Alternative Form 2 is used because of the specified additional hinge modes and external damping forces. In the case of multiple machines, another Alternative Form 3 is used because it calls upon the initial .frc file for each body, thus simplifying input parameters.

The mass and inertia matrix is input for the 6 standard rigid body motions as well as the 3 added hinges motions. The 6x6 portion of the matrix for the standard rigid body motions simplifies because the center of mass is assumed to be at the origin and the motions are limited to those in the vertical plane.

Surge, Heave and Pitch for standard rigid body motions, along with the 3 added vertical hinge modes. The matrix has the non-zero elements shown below:

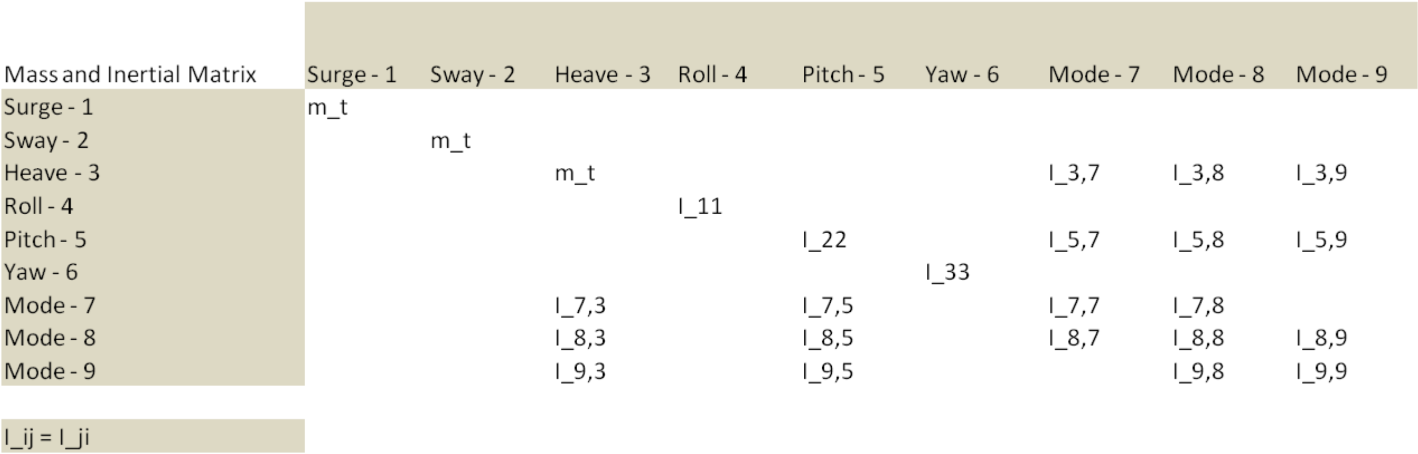

Mass and Inertial Matrix	Surge - 1	Sway - 2	Heave - 3	Roll - 4	Pitch - 5	Yaw - 6	Mode - 7	Mode - 8	Mode - 9
Surge - 1	m_t								
Sway - 2		m_t							
Heave - 3			m_t				I_3,7	I_3,8	I_3,9
Roll - 4				I_11					
Pitch - 5					I_22		I_5,7	I_5,8	I_5,9
Yaw - 6						I_33			
Mode - 7			I_7,3		I_7,5		I_7,7	I_7,8	
Mode - 8			I_8,3		I_8,5		I_8,7	I_8,8	I_8,9
Mode - 9			I_9,3		I_9,5			I_9,8	I_9,9

I_ij = I_ji

Table 1: Mass and Inertia Matrix

The 6x6 portion for standard rigid body motions is solved for using methods from Newman6. In the matrix, m_t represents the total mass while $I_{11,22,33}$ are moments of inertia:

$$I_{ij} = \iiint_{V_b} \rho_b \left[\boldsymbol{x} \cdot \boldsymbol{x} \delta_{ij} - \boldsymbol{x}_i \boldsymbol{x}_j \right] dV \qquad (4.1)$$

The added mode terms can be solved using the method of weighted residuals[7]:

$$M_{ij} = \int_{-L/2}^{L/2} m f_i(x) f_j(x) dx \qquad (4.2)$$

$$I_{ij} = \iiint_{-L/2}^{L/2} m f_i(x) f_j(x) dV \qquad (4.3)$$

Many of the added mode terms simplify:

Mass and Inertial Matrix	Surge - 1	Sway - 2	Heave - 3	Roll - 4	Pitch - 5	Yaw - 6	Mode - 7	Mode - 8	Mode - 9
Surge - 1	m_t								
Sway - 2		m_t							
Heave - 3			m_t				(m_1+m_2)/2	(m_2+m_3)/2	(m_3+m_4)/2
Roll - 4				I_11					
Pitch - 5					I_22		I_5,7	I_5,8	I_5,9
Yaw - 6						I_33			
Mode - 7			(m_1+m_2)/2		I_7,5		(m_1+m_2)/3	(1/6)m_2	
Mode - 8			(m_2+m_3)/2		I_8,5		(1/6)m_2	(m_2+m_3)/3	(1/6)m_3
Mode - 9			(m_3+m_4)/2		I_9,5			(1/6)m_3	(m_3+m_4)/3
I_ij = I_ji									

Table 2: Simplified Mass and Inertia Matrix

The only terms that are numerically integrated are related to the Pitch modes, as visualized in Figure 11.

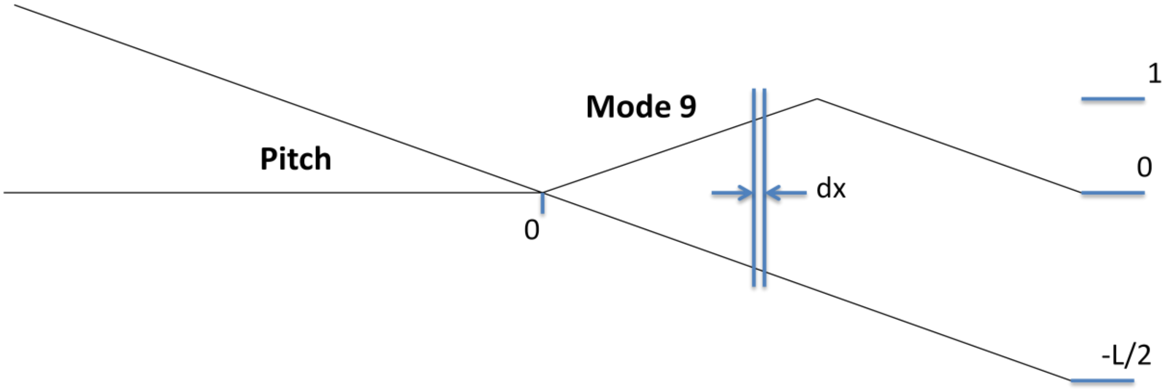

Figure 11: Pitch Mode Integration

Once this 9x9 Mass and Inertia Matrix is determined, it is input into the .FRC text file. Along with this, the Damping Matrix is input into the .FRC file. The Damping Matrix is solved for using a methodology presented by Peter Anast[8] in a paper describing performance trends of hinged raft WECs and based on a suggestion by Newman[9]. This process is based on a linear relationship between hinge angular velocities that generate resistive tensional damping and hinge modal velocities. The method is as follows[8]:

Assume angles are small such that sinθ≈θ.

$$\theta_i = \sum_{j=1}^{n} A_{ij} X_j \tag{4.4}$$

θ_i is the hinge angle as a function of X_j, the modal displacement at the jth hinge and n is the number of hinges.

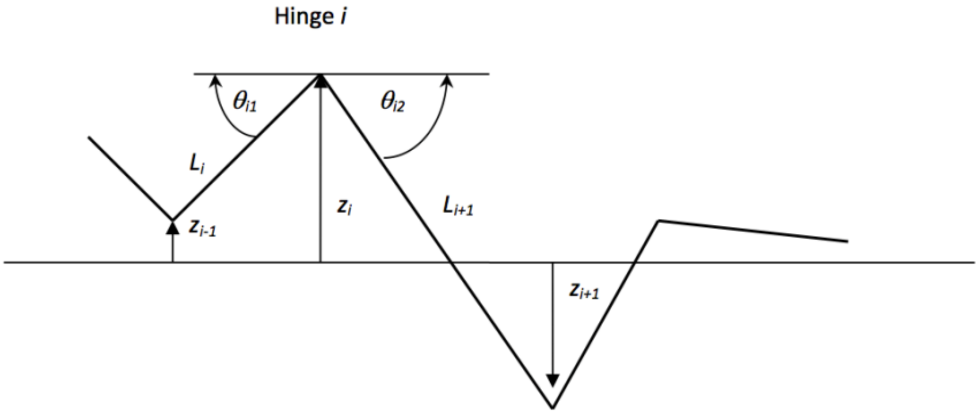

Figure 12: Hinge Angle θ_i Schematic

The hinge angle θ_i is the sum of two components, θ_{i1} and θ_{i2}. Calling z_i the vertical displacement at a raft end corresponding to the ith hinge, we have:

$$\theta_i = \frac{z_i - z_{i-1}}{L_i} + \frac{z_i - z_{i+1}}{L_{i+1}} \tag{4.5}$$

Because of WAMIT™'s pitch convention, β is defined as the opposite of the pitch angle and h the heave displacement for the overall (rigid) system of length L, gives:

$$z_i = h + x_i\beta + X_i \tag{4.6}$$

where x_i is the longitudinal coordinate of the ith hinge, for i=1,...,n, while:

$$z_o = h - \frac{L}{2}\beta \tag{4.7}$$

$$z_{n+1} = h + \frac{L}{2}\beta \tag{4.8}$$

Substituting these expressions in Equation (4.5), it is clear that the rigid-body mode contributions cancel out, as expected, and that the only non-zero coefficients in Equation (4.4) are:

$$\begin{cases} a_{ii} = \frac{1}{L_i} + \frac{1}{L_{i+1}} \\ a_{ij} = a_{ji} = -\frac{1}{L_{Max(i,j)}} \end{cases} \quad \text{when both i≠j and Max(i,j)=Min(i,j)+1} \tag{4.9}$$

The power extracted by the linear torsional damping mechanisms, which exert resistive torques equal to $-b_k\dot{\theta}_k$ is equal to:

$$P = \sum_{k=1}^{n} b_k \dot{\theta}_k^2 = \sum_{k=1}^{n} b_k \left(\sum_{i=1}^{n} a_{ki} \dot{X}_i \right) \left(\sum_{j=1}^{n} a_{kj} \dot{X}_j \right) \tag{4.10}$$

The second equality makes use of equation (4.4) and the dummy indices have been selected to facilitate the determination of the external damping matrix below.

In WAMIT™, external damping forces F_i are expressed in terms of the external damping matrix coefficients B_{ij} and the hinge modal velocities $\dot{X}_j$ as:

$$F_i = -\sum_{j=1}^{n} B_{ij} \dot{X}_j \tag{4.11}$$

The power extraction corresponding to such forces is equal to:

$$P = \sum_{i=1}^{n} \left(\sum_{j=1}^{n} B_{ij} \dot{X}_j \right) \dot{X}_i \tag{4.12}$$

Comparing Equations (4.10) and (4.12) leads to:

$$B_{ij} = \sum_{k=1}^{n} b_k a_{ki} a_{kj} \tag{4.13}$$

Equation (4.13) shows the matrix for the external damping. This matrix becomes a function of b, the torsional damping coefficient. Once put into a 9x9 form for WAMIT™ input, it becomes:

Damp Matrix	Surge - 1	Sway - 2	Heave - 3	Roll - 4	Pitch - 5	Yaw - 6	Mode - 7	Mode - 8	Mode - 9
Surge - 1									
Sway - 2									
Heave - 3									
Roll - 4									
Pitch - 5									
Yaw - 6									
Mode - 7							(5*b)/(L^2)	(-4*b)/(L^2)	
Mode - 8							(-4*b)/(L^2)	(6*b)/(L^2)	(-4*b)/(L^2)
Mode - 9								(-4*b)/(L^2)	(5*b)/(L^2)

Figure 13: External Damping Matrix

CFG:

The .cfg file is used to specify various configuration parameters associated with the specifics of the run. This includes number of CPUs, RAM, methods used for body input, solving method as well as any additional specifics needed. For this study, the file includes the definition of the Low Order method, calling upon built-in added hinge modes, definition of alternative .frc file and multiple body options. The built in .dll file for the hinge modes is modified to accommodate multiple bodies. Output of WAMIT™ is in the form of .txt files according to input specifics. These are easily read into MATLAB and Microsoft Excel for post processing.

5. Test 24

In order to first confirm the methodology used, a comparison of RAO motion of a WAMIT™ given example, Test 24, is made. The Test 24 body shape is that of a hinged raft with 4 hinges and an overall length of 20m, as shown in Figure 14.

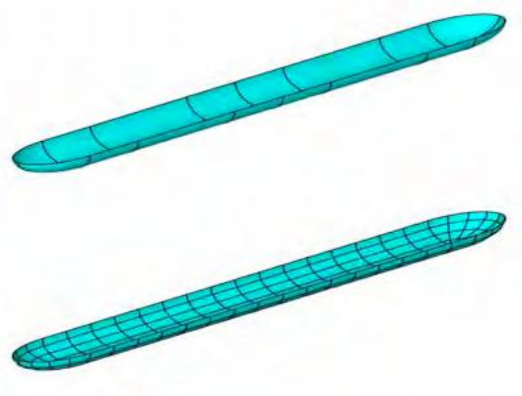

Figure 14: WAMIT™ Test 24 hinged raft[5]

This WAMIT™ given example uses built in geometry as well as symmetry when defining its mesh and solves for the potential using the 'High Order' panel method. The added modes use symmetry as well, calling upon the built in added hinge mode functions. These modes are broken into symmetric and antisymmetric shapes as seen down the right hand side of Figure 15. This symmetry helps to decrease run time.

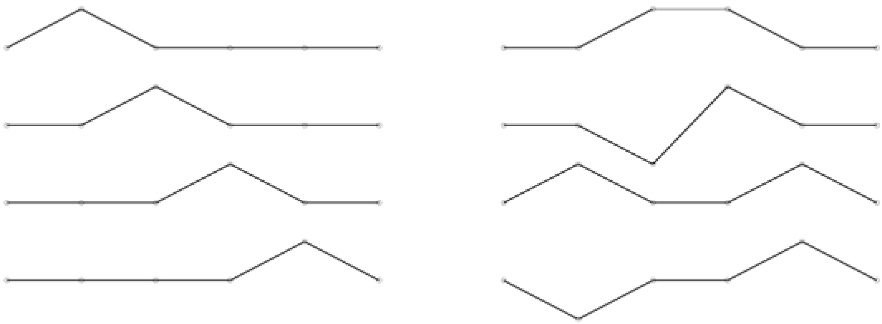

Figure 15: WAMIT™ defined Hinge Modes

The methodology used for the P1 shape is applied to Test 24. The difference between the given WAMIT™ test and the P1 simulation is use of the 'Low Order' method to solve for the potential, a mesh uploaded in the input files, and 'tent' mode shapes as shown on the left hand side of Figure 15. Both methods do not include an external damping matrix. In order to compare the two methods, the RAOs of individual hinges are computed and show excellent agreement:

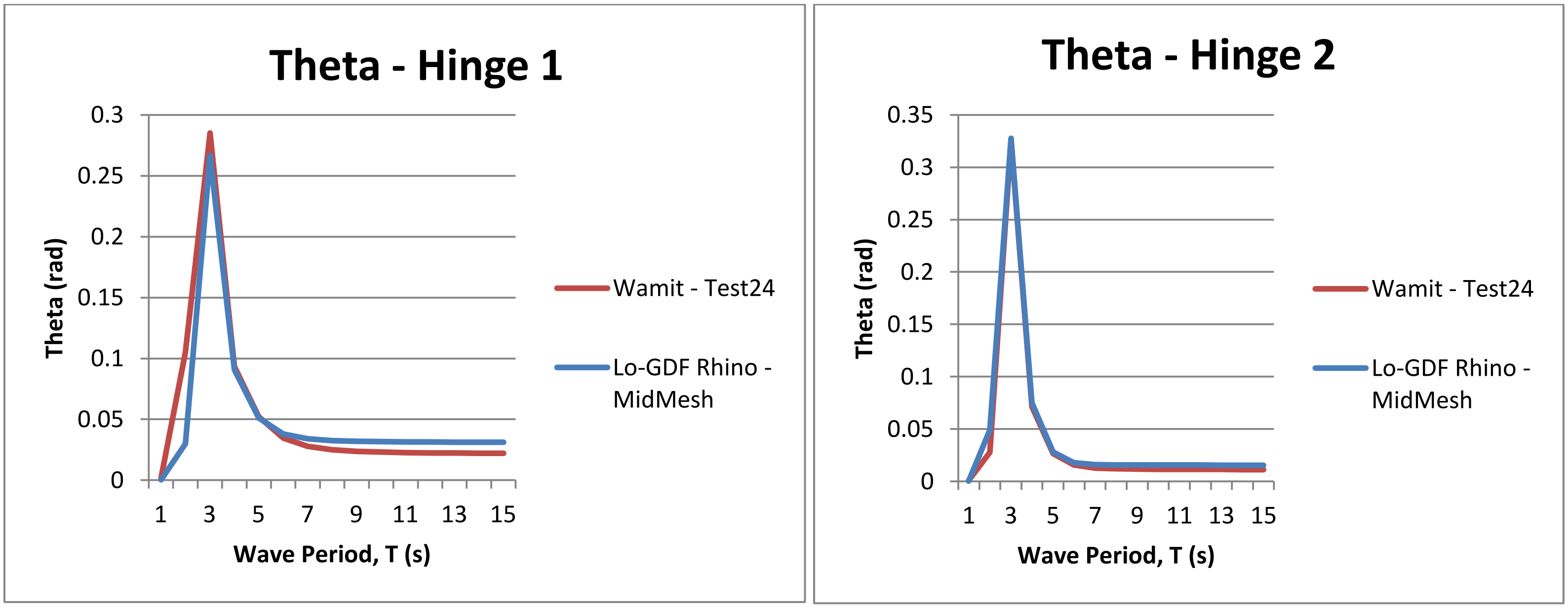

Figure 16:Test 24 Hinge1 &2 RAO comparison

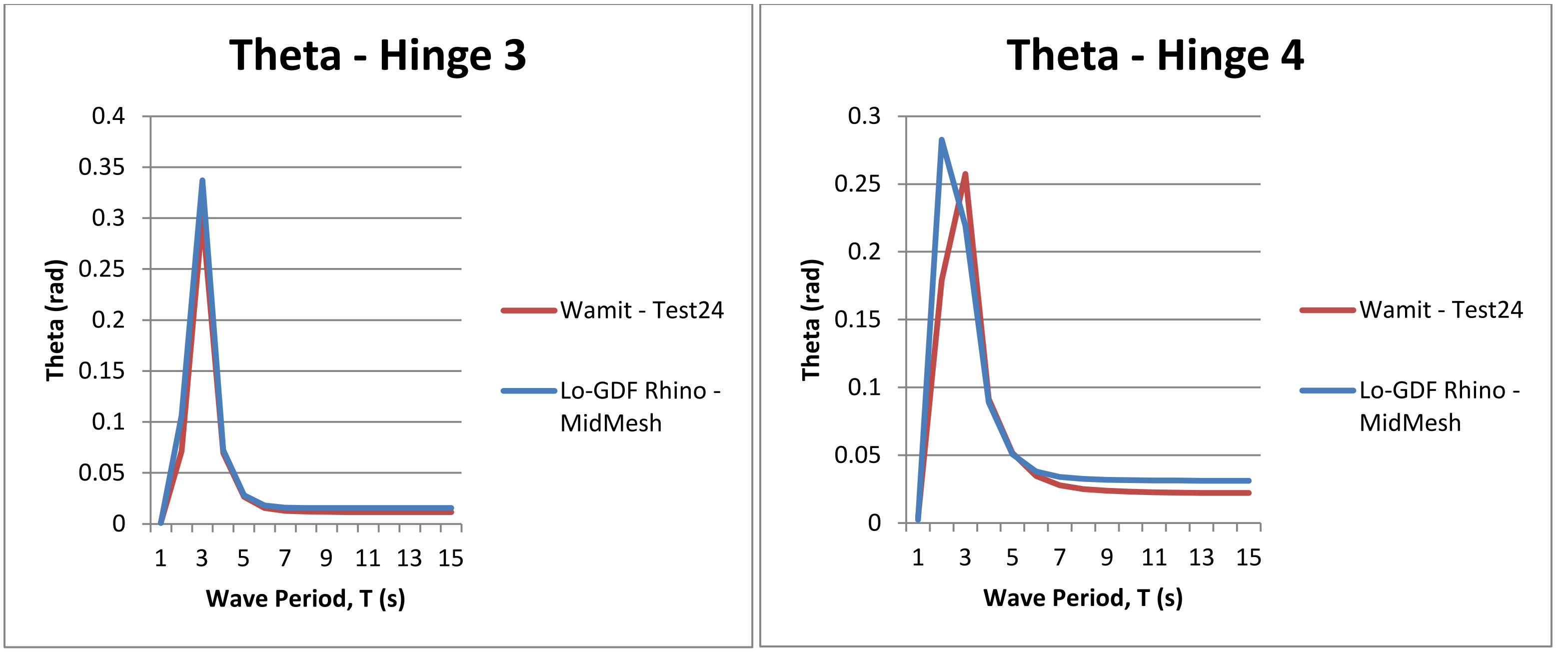

Figure 17:Test 24 Hinge3&4 RAO comparison

This confirms the methodology to be used for the P1 WEC.

6. Power Take Off

Power take off on the hinges is calculated using a relationship between the change in hinge angle θ and the damping coefficient used at each hinge, b.

Starting in time domain:

$$P = b\dot{\theta}^2 \tag{6.1}$$

Where:

$$\dot{\theta} = A\,\Re\{i\omega\bar{\theta}e^{i\omega t}\} \tag{6.2}$$

Substitute (6.2) into (6.1)

$$P(t) = A^2 b[\Re\{i\omega\bar{\theta}e^{i\omega t}\}]^2 \tag{6.3}$$

Average over one period:

$$\begin{aligned}\bar{P} &= A^2 b\frac{1}{T}\int_0^T [\Re\{i\omega\bar{\theta}e^{i\omega t}\}]^2\,dt \\ &= A^2 b\frac{1}{2}\Re\{-i^2\omega^2\bar{\theta}^2\}\end{aligned} \tag{6.4}$$

The resulting power from a monochromatic wave is therefore:

$$P = \frac{1}{2}A^2 b\omega^2|\theta|^2 \tag{6.5}$$

Power flux per unit width of monochromatic wave:

$$P_o = \frac{\rho g^2 H_s^2 T_e}{64\pi}$$

$$P_o(\omega) = \frac{\rho g^2 (2A)^2}{16\omega} \tag{6.6}$$

Power flux per unit width of wave crest from the spectrum:

$$P_o = \rho g \int_0^\infty S(\omega) c_g d\omega = \sum \frac{\rho g^2 S(\omega) d\omega}{2\omega} \tag{6.7}$$

Substituting equation (6.7) for each hinge angle, the average power from each hinge for each heading wave is:

$$\overline{P} = \sum_{\omega} b|\theta|^2 \omega^2 S(\omega) d\omega \tag{6.8}$$

A Bretschneider spectrum is used:

$$S(\omega) = \frac{5}{16} H_s^2 \frac{\omega_p^4}{\omega^5} e^{\left[-\frac{5}{4}\left(\frac{\omega_p}{\omega}\right)^4\right]} \tag{6.9}$$

This is discretized at intervals of .5 seconds but because dω is not constant, it needs to be adjusted for integration. This is because of a steep slope at low frequencies as seen on the spectrum plot in Figure 18. An averaging method[8] is used to solve for the width, dω, at each interval.

$$lo(T) = \frac{(\omega(T) + \omega(T + .5))}{2} \tag{6.10}$$

$$hi(T) = \frac{(\omega(T) + \omega(T - .5))}{2} \tag{6.11}$$

$$Width = hi(T) - lo(T) \tag{6.12}$$

This results in a better width spacing for the integration summation. This is shown in Table 3 for T_p=8s and H_s=4m, and in Figure 18, along with the spectrum and integration approximation.

Bretschneider Spectrum					For T_p=8s and H_s=4m
T	ω	ωHi(T)	Lo(T)	dω	S(ω)
1	6.283185	9.424778	5.235988	4.18879	0.000106
1.5	4.18879	5.235988	3.665191	1.570796	0.000806
2	3.141593	3.665191	2.827433	0.837758	0.003392
2.5	2.513274	2.827433	2.303835	0.523599	0.010311
3	2.094395	2.303835	1.944795	0.359039	0.025478
3.5	1.795196	1.944795	1.682996	0.261799	0.054436
4	1.570796	1.682996	1.48353	0.199466	0.104271
4.5	1.396263	1.48353	1.32645	0.15708	0.183129
5	1.256637	1.32645	1.199517	0.126933	0.299201
5.5	1.142397	1.199517	1.094797	0.10472	0.459089
6	1.047198	1.094797	1.006921	0.087877	0.665614
6.5	0.966644	1.006921	0.932121	0.0748	0.915328
7	0.897598	0.932121	0.867678	0.064443	1.196315
7.5	0.837758	0.867678	0.811578	0.0561	1.487103
8	0.785398	0.811578	0.762298	0.04928	1.757602
8.5	0.739198	0.762298	0.718665	0.043633	1.972753
9	0.698132	0.718665	0.67976	0.038905	2.098818
9.5	0.661388	0.67976	0.644853	0.034907	2.111244
10	0.628319	0.644853	0.613359	0.031495	2.001891
10.5	0.598399	0.613359	0.584799	0.02856	1.782988
11	0.571199	0.584799	0.558781	0.026017	1.485727
11.5	0.546364	0.558781	0.534981	0.0238	1.15322
12	0.523599	0.534981	0.513127	0.021855	0.829859
12.5	0.502655	0.513127	0.492988	0.020138	0.550801
13	0.483322	0.492988	0.474372	0.018617	0.335363

Table 3: Integral Intervals S(ω)

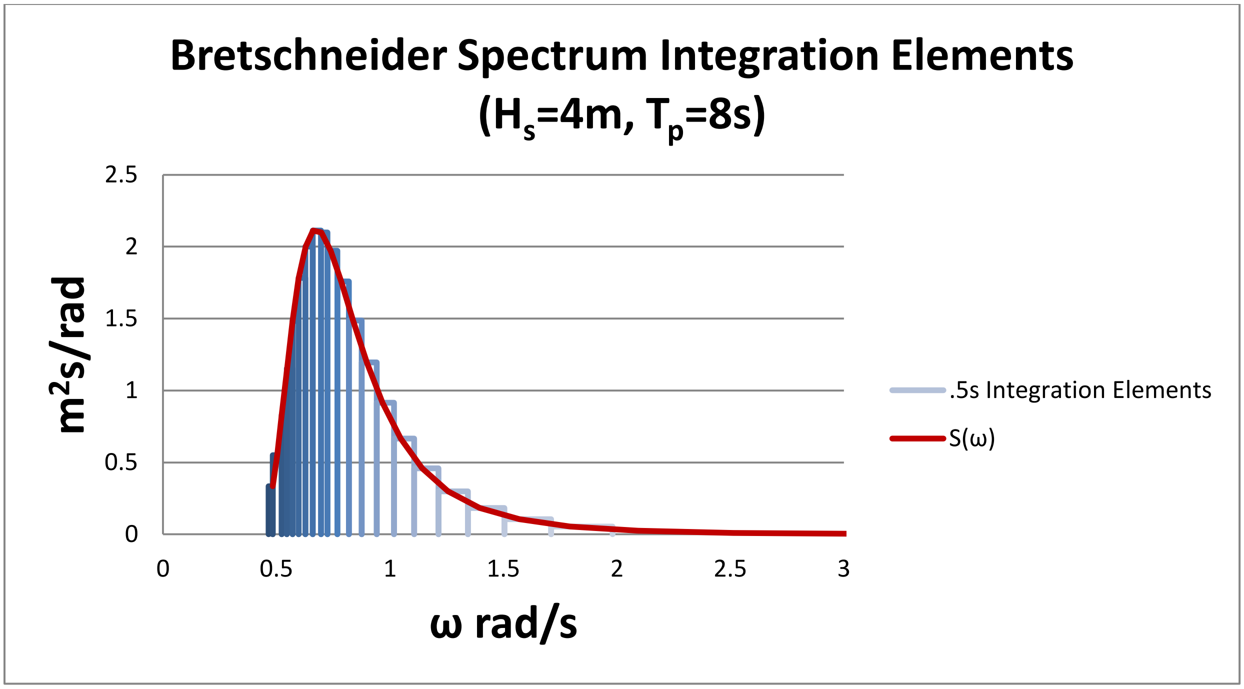

Figure 18: Bretschneider Spectrum Integration Elements

The spectrum to be applied is defined by significant wave height and peak period, but the Matrix to be recreated is defined with conditions of significant wave height and power or energy period (T_p or T_e). The deep-water energy period of a sea state is defined in terms of spectral moments as:

$$T_e = \frac{m_{-1}}{m_0} = \frac{\int_0^{2\pi}\int_0^{\infty} f^{-1}S(f)df d\theta}{\int_0^{2\pi}\int_0^{\infty} S(f)df d\theta} \qquad (6.13)$$

For a given spectral shape this can be given in relation to T_p:

$$T_e = \alpha T_p \qquad (6.14)$$

where α is a factor based on the shape of the wave spectrum, which increases toward unity with decreasing spectral width. As noted in a Global Wave Energy Resource Assessment[11], the coefficient for the Pierson-Moskowitz and Bretschneider Spectra is α=.86.

7. Damping

In order to represent a power take off from the calculations in the previous chapter, a damping factor, b, needs to be chosen. This value affects the external damping matrix and power take off calculations. A range of values for the coefficient is chosen, based on similar devices[1], in order to compare power and motion RAOs, ≈10e6-10e11 (N·m·s). Running many tests allows for good post processing comparison of outputs. These outputs will be a function not only of the damping coefficient but also of wave period. The range of periods is based on the values in the published targeted power matrix, T_e= 6.5s-12s. A wave height is chosen for analysis, but this is insignificant to determine trends in power production, as it only effects a scaling of the overall values.

Ideally, there should be a peak in power production for all conditions at a single damping coefficient. The plots of Power (blue) and RAOs (red, green, purple) as a function of the damping coefficient,b, are shown in Figure 19Figure 20 for two values of T_e (the damping coefficient is plotted on a log scale):

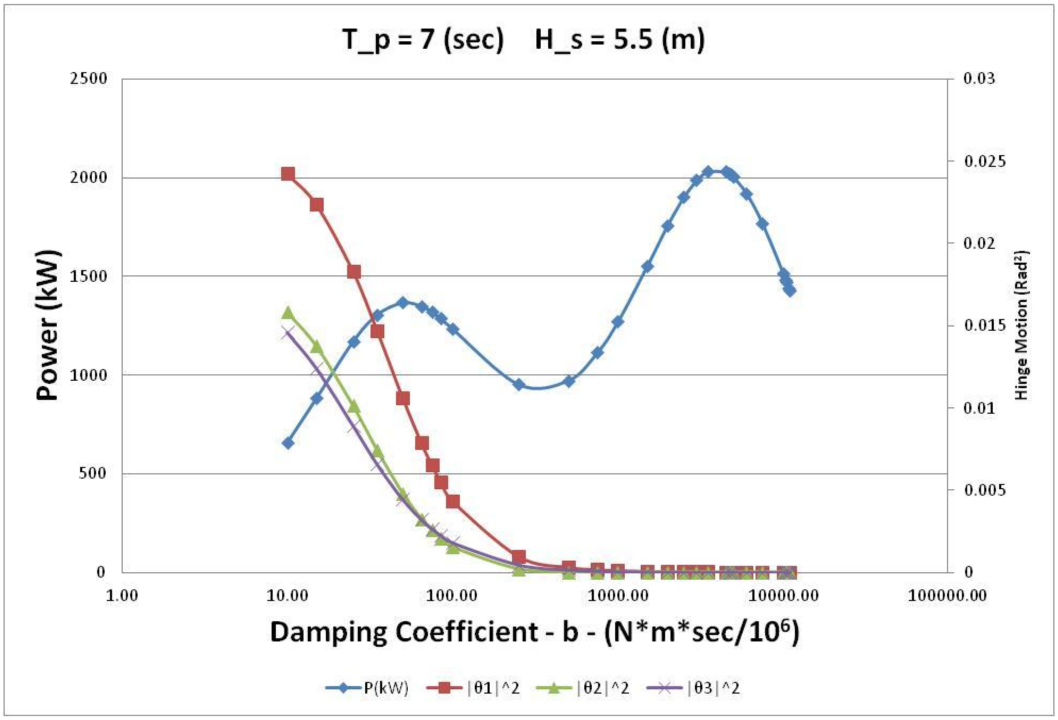

Figure 19: Power (blue) and RAOs (red, green, purple) as functions of Damping coefficient - T_e=7s

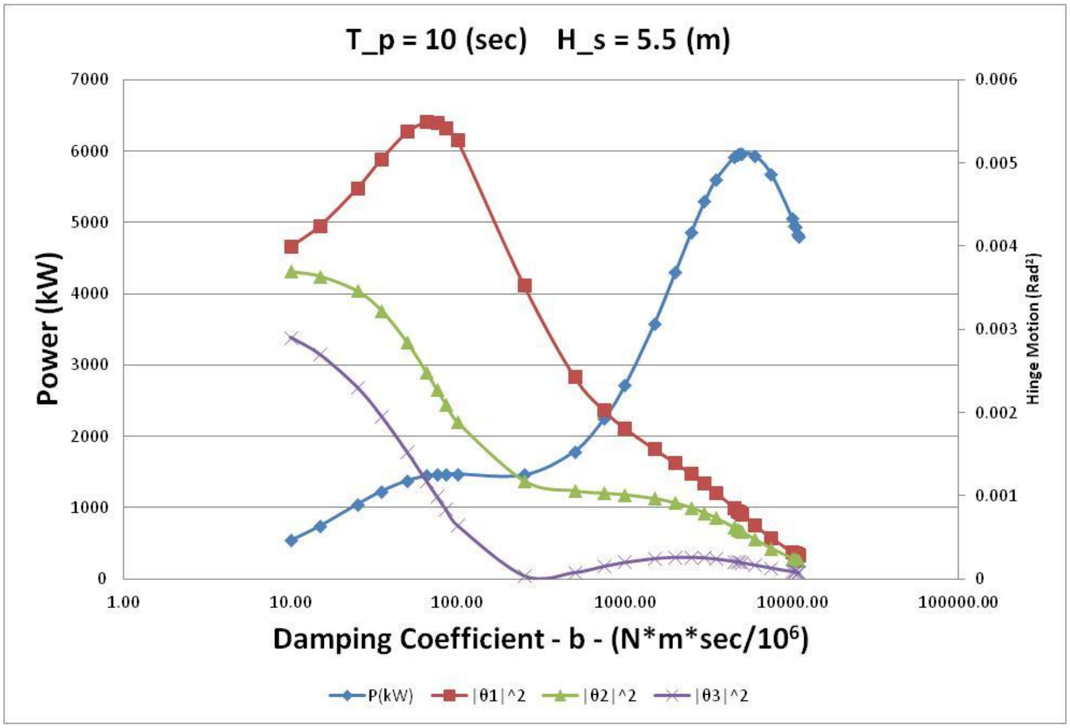

Figure 20: Power (blue) and RAOs (red, green, purple) as functions of Damping coefficient - T_e=10s

At T_e=7s, as shown in Figure 19, there are two power peaks. But the RAOs decline to zero at the higher damping values. This might indicate a false power peak at high damping. As T_e is increased, the higher damping peak becomes larger, as shown in Figure 20. Again, the motions are very small at higher damping values. This second peak may not be realistic, and caused by a 0x∞ type of error in calculation, meaning that the large damping values are being multiplied by the very small hinge motion amplitude RAOs. To confirm this theory, another plot was made similar to Figure 19 andFigure 20, but instead of the RAOs, it shows all the terms in the power calculation except for the damping coefficient, or the ratio Power/Damping Coefficient. Shown in Figure 21 andFigure 22 are the plots for the same wave periods, T_e=7 and 10s.

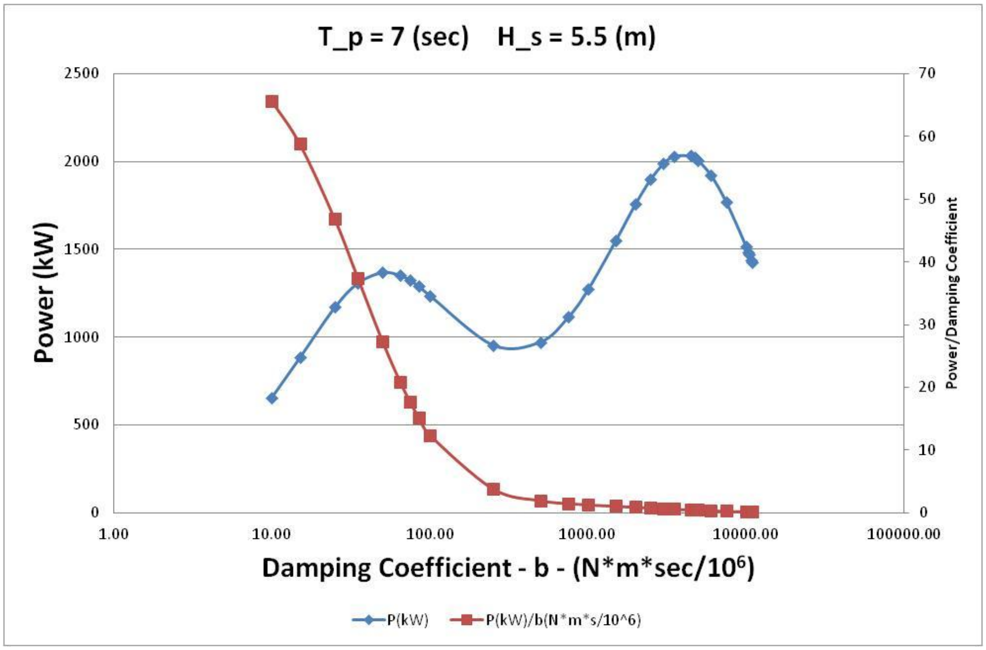

Figure 21: Power (blue) and Power/Damping Coefficient (red) as functions of Damping coefficient - Te=7s

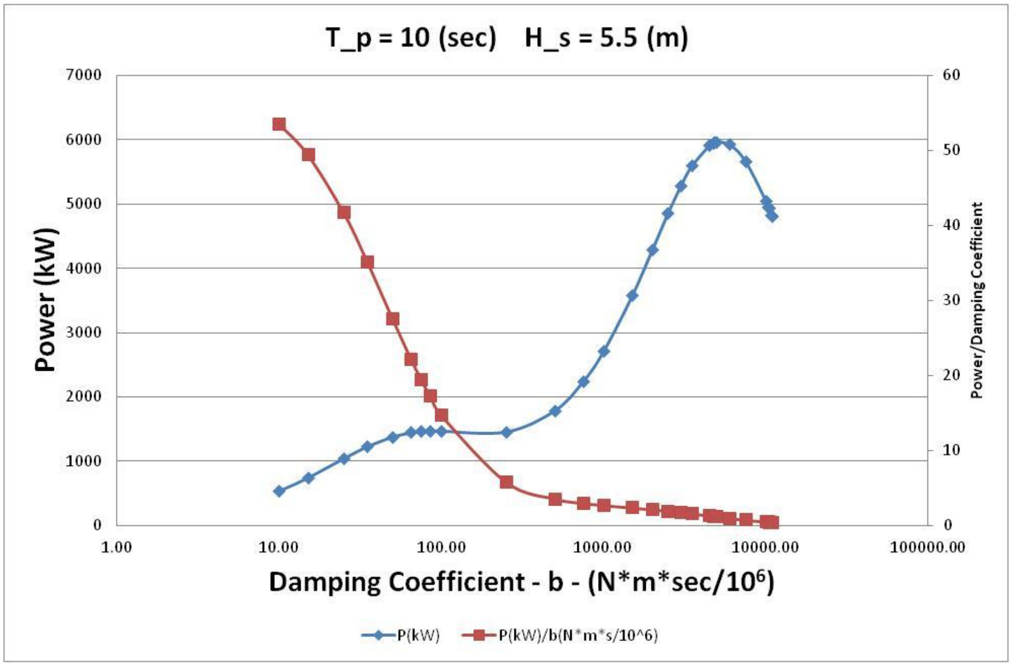

Figure 22: Power (blue) and Power/Damping Coefficient (red) as functions of Damping coefficient - Te=10s

This confirms the 0x∞ suspicion, as in both Figure 21 andFigure 22, the Power/Damping coefficient terms go to zero at higher damping coefficients. This is unrealistic because at such high damping values, the machine essentially would not move, as demonstrated in Figure 19 andFigure 20, and thus the hydraulic pistons would not pump the hydraulic fluid needed to turn the generators for the machine.

This suggests that the first power peak is the good choice for b. The corresponding value of b stays at approximately 6.5x10^7 (N·m·s) throughout the range of T_e. Ideally, this damping value would be changed to match the wave conditions the machine is seeing when in the field, in order to maximize output. But for simplicity in this study, b=6.5x10^7 (N·m·s) will be held constant for all hinges on the single machine as well as for the multiple machine tests.

8. Single Machine

With the damping coefficient chosen and held constant, power can be calculated for many different wave conditions. With this, a power matrix can be created for the hydrodynamic power output. This is the amount of power theoretically absorbed by the hinge motions without any subsequent losses.

WAMIT Calculated(kW)	5	5.5	6	6.5	7	7.5	8	8.5	9	9.5	10	10.5	11	11.5	12	12.5	13	T_e
0.5																		
1		34.0	44.3	51.2	54.4	54.4	52.2	48.6	44.3	39.8	35.3	31.2	27.5	24.1				
1.5	49.9	76.5	99.6	115.2	122.3	122.4	117.4	109.3	99.6	89.4	79.5	70.3	61.8	54.3	47.6	41.8	36.7	750(kW) Max
2	88.6	135.9	177.1	204.7	217.5	217.6	208.7	194.2	177.0	159.0	141.4	124.9	109.9	96.5	84.6	74.2	65.2	
2.5	138.5	212.4	276.7	319.9	339.8	340.0	326.1	303.5	276.6	248.4	220.9	195.2	171.7	150.7	132.2	116.0	101.9	
3	199.4	305.8	398.4	460.7	489.4	489.6	469.5	437.0	398.3	357.8	318.1	281.0	247.3	217.1	190.4	167.0	146.7	
3.5		416.3	542.2	627.0	666.1	666.4	639.1	594.8	542.1	486.9	433.0	382.5	336.5	295.4	259.1	227.4	199.7	
4			708.2	819.0	870.0	870.4	834.7	776.9	708.1	636.0	565.6	499.6	439.6	385.9	338.5	297.0	260.8	
4.5			896.4	1036.5	1101.1	1101.6	1056.4	983.3	896.2	804.9	715.8	632.3	556.3	488.4	428.4	375.8	330.1	
5				1279.6	1359.4	1360.0	1304.2	1213.9	1106.4	993.8	883.7	780.6	686.8	602.9	528.9	464.0	407.5	
5.5				1548.4	1644.8	1645.6	1578.1	1468.9	1338.8	1202.5	1069.3	944.6	831.0	729.5	639.9	561.4	493.0	
6					1957.5	1958.4	1878.1	1748.1	1593.2	1431.0	1272.5	1124.1	989.0	868.2	761.6	668.1	586.8	
6.5					2297.3	2298.4	2204.1	2051.5	1869.8	1679.5	1493.4	1319.3	1160.7	1018.9	893.8	784.1	688.6	
7						2665.6	2556.3	2379.3	2168.6	1947.8	1732.0	1530.1	1346.1	1181.7	1036.6	909.4	798.6	
7.5							2934.5	2731.3	2489.4	2236.0	1988.3	1756.5	1545.3	1356.6	1189.9	1044.0	916.8	
8								3107.7	2832.4	2544.0	2262.3	1998.5	1758.2	1543.5	1353.9	1187.8	1043.1	
H_s																		

Figure 23: Calculated Hydrodynamic Power Matrix, No Losses

% of Pelamis brochure value	5	5.5	6	6.5	7	7.5	8	8.5	9	9.5	10	10.5	11	11.5	12	12.5	13	T_e
0.5																		
1		154.5	152.6	150.5	147.0	143.2	137.3	131.2	126.4	124.2	121.9	120.1	119.4	114.8				
1.5	155.8	152.9	153.2	151.5	147.4	142.3	136.5	131.6	127.7	124.2	122.4	119.1	116.6	115.5	113.3	112.9	111.1	
2	155.5	154.5	154.0	150.5	147.0	142.2	137.3	132.1	128.3	125.2	121.9	120.1	118.2	116.2	114.3	112.5	110.5	750(kW
2.5	155.6	153.9	153.7	150.9	147.1	142.9	137.0	131.9	128.1	124.8	122.1	119.7	117.6	115.9	114.0	112.6	110.7	
3	154.6	154.5	153.2	151.0	147.4	144.0	141.4	138.7	136.4	134.5	132.6	128.3	117.7	115.5	114.0	112.1	111.1	
3.5		154.2	153.2	151.1	152.1	151.5	150.7	147.2	143.8	134.5	132.8	131.0	129.4	128.4	120.5	112.6	110.9	
4			153.3	163.1	161.1	159.4	157.5	155.7	149.1	148.3	147.3	136.5	129.7	128.2	126.8	125.3	122.4	
4.5			164.8	163.2	171.5	170.0	168.2	166.7	159.5	152.5	151.3	146.4	145.6	137.2	126.7	125.3	124.1	
5				173.2	187.2	186.0	184.5	176.7	165.1	163.7	158.7	149.8	145.5	144.6	143.3	133.3	124.2	
5.5				206.4	219.3	219.4	210.4	195.8	181.6	180.3	162.5	161.2	156.8	147.1	143.5	142.1	138.9	
6					261.0	261.1	250.4	233.1	212.4	190.8	179.0	177.6	159.8	155.6	148.7	142.2	141.4	
6.5					306.3	306.5	293.9	273.5	249.3	223.9	199.1	177.6	176.4	164.1	154.4	153.2	143.2	
7						355.4	340.8	317.2	289.1	259.7	230.9	204.0	179.5	174.8	169.1	155.7	152.1	
7.5							391.3	364.2	331.9	298.1	265.1	234.2	206.0	180.9	173.5	167.8	154.6	
8								414.4	377.7	339.2	301.6	266.5	234.4	205.8	180.5	172.1	166.9	
H_s																		

Figure 24: Percentage of Pelamis® Targeted Power Matrix - Hydrodynamic, no losses

Shown in Figure 23 is the Calculated Hydrodynamic Power Matrix, and below in Figure 24, is the corresponding percentage of the targeted power matrix. The cells highlighted in orange represent the cut-off or saturation zone in which Pelamis® targeted power is capped at 750kW. The Hydrodynamic Power Matrix values are larger, in some cases 400% larger. Such a large scale of difference can be anticipated as various losses not taken into account. These include, mechanical losses, most likely from the pistons and generator, electrical losses, from transport and conversion, and the generator cut-off or saturation conditions. These losses need to approximated in order to get a realistic yearly average power output. With no information given from Pelamis® on the specifics of losses, they can be approximated in a few different ways. The first step though, will be to approximate the saturation or cut-off conditions, shown in orange. This is done by averaging the boundary values of the saturation zone and setting the entire zone to this value.

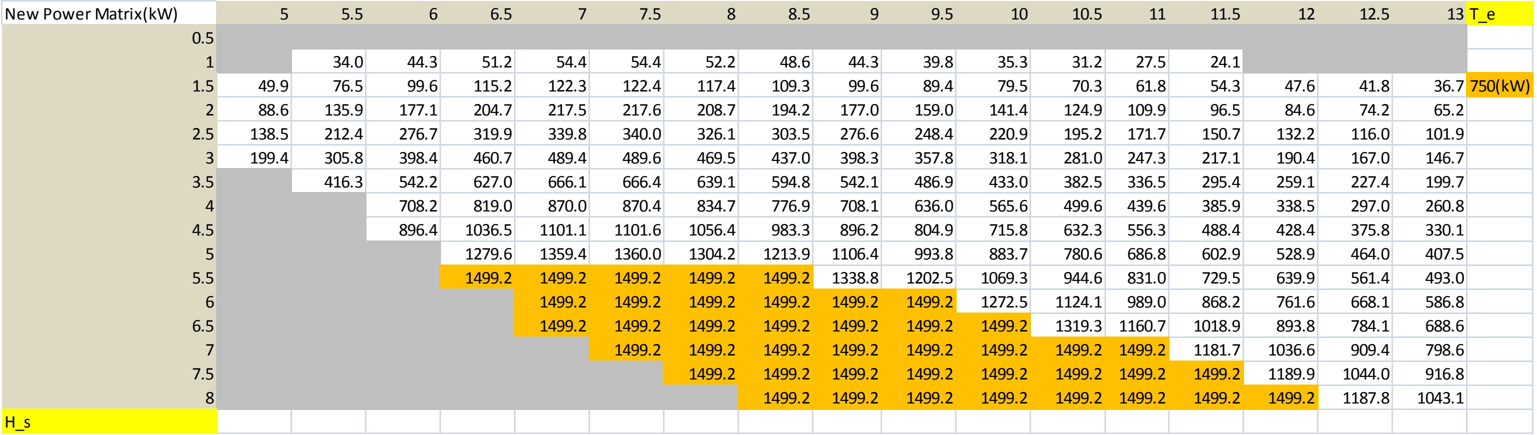

New Power Matrix(kW)	5	5.5	6	6.5	7	7.5	8	8.5	9	9.5	10	10.5	11	11.5	12	12.5	13	T_e
0.5																		
1		34.0	44.3	51.2	54.4	54.4	52.2	48.6	44.3	39.8	35.3	31.2	27.5	24.1				
1.5	49.9	76.5	99.6	115.2	122.3	122.4	117.4	109.3	99.6	89.4	79.5	70.3	61.8	54.3	47.6	41.8	36.7	750(kW)
2	88.6	135.9	177.1	204.7	217.5	217.6	208.7	194.2	177.0	159.0	141.4	124.9	109.9	96.5	84.6	74.2	65.2	
2.5	138.5	212.4	276.7	319.9	339.8	340.0	326.1	303.5	276.6	248.4	220.9	195.2	171.7	150.7	132.2	116.0	101.9	
3	199.4	305.8	398.4	460.7	489.4	489.6	469.5	437.0	398.3	357.8	318.1	281.0	247.3	217.1	190.4	167.0	146.7	
3.5		416.3	542.2	627.0	666.1	666.4	639.1	594.8	542.1	486.9	433.0	382.5	336.5	295.4	259.1	227.4	199.7	
4			708.2	819.0	870.0	870.4	834.7	776.9	708.1	636.0	565.6	499.6	439.6	385.9	338.5	297.0	260.8	
4.5			896.4	1036.5	1101.1	1101.6	1056.4	983.3	896.2	804.9	715.8	632.3	556.3	488.4	428.4	375.8	330.1	
5				1279.6	1359.4	1360.0	1304.2	1213.9	1106.4	993.8	883.7	780.6	686.8	602.9	528.9	464.0	407.5	
5.5				1499.2	1499.2	1499.2	1499.2	1499.2	1338.8	1202.5	1069.3	944.6	831.0	729.5	639.9	561.4	493.0	
6					1499.2	1499.2	1499.2	1499.2	1499.2	1499.2	1272.5	1124.1	989.0	868.2	761.6	668.1	586.8	
6.5					1499.2	1499.2	1499.2	1499.2	1499.2	1499.2	1499.2	1319.3	1160.7	1018.9	893.8	784.1	688.6	
7						1499.2	1499.2	1499.2	1499.2	1499.2	1499.2	1499.2	1499.2	1181.7	1036.6	909.4	798.6	
7.5							1499.2	1499.2	1499.2	1499.2	1499.2	1499.2	1499.2	1499.2	1189.9	1044.0	916.8	
8								1499.2	1499.2	1499.2	1499.2	1499.2	1499.2	1499.2	1499.2	1187.8	1043.1	
H_s																		

Figure 25: Hydrodynamic Power Matrix - Cut-off/Saturation loss applied

Figure 25 shows the new calculated Hydrodynamic Power Matrix with the saturation zone approximated as one value. This cut-off limit will be held for the remaining tests in the study.

The other losses that need to be accounted for, mechanical, electrical and others, can be approximated as one loss variable. This variable will be a ratio of the hydrodynamic power output to the final approximated power output. There are a few methods to do this, and the following are considered:

1. Single value based on cut off average:

This method uses one ratio based on the saturation average to the published saturation values. The ratio is 750kW/1499.2 kW= 1/1.999 and is applied to the entire matrix:

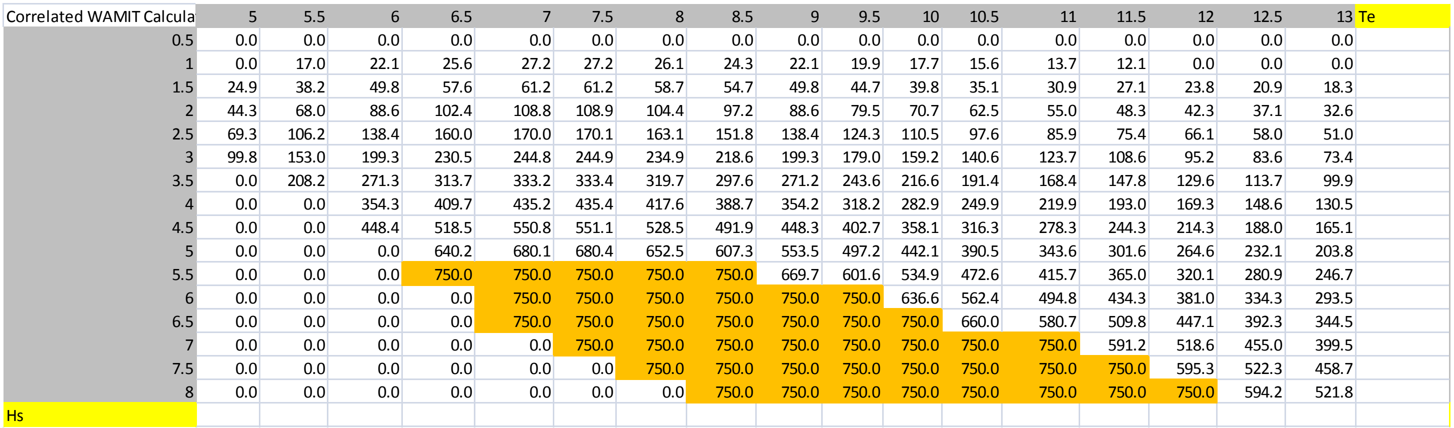

Correlated WAMIT Calcula	5	5.5	6	6.5	7	7.5	8	8.5	9	9.5	10	10.5	11	11.5	12	12.5	13	Te
0.5	0.0	0.0	0.0	0.0	0.0	0.0	0.0	0.0	0.0	0.0	0.0	0.0	0.0	0.0	0.0	0.0	0.0	
1	0.0	17.0	22.1	25.6	27.2	27.2	26.1	24.3	22.1	19.9	17.7	15.6	13.7	12.1	0.0	0.0	0.0	
1.5	24.9	38.2	49.8	57.6	61.2	61.2	58.7	54.7	49.8	44.7	39.8	35.1	30.9	27.1	23.8	20.9	18.3	
2	44.3	68.0	88.6	102.4	108.8	108.9	104.4	97.2	88.6	79.5	70.7	62.5	55.0	48.3	42.3	37.1	32.6	
2.5	69.3	106.2	138.4	160.0	170.0	170.1	163.1	151.8	138.4	124.3	110.5	97.6	85.9	75.4	66.1	58.0	51.0	
3	99.8	153.0	199.3	230.5	244.8	244.9	234.9	218.6	199.3	179.0	159.2	140.6	123.7	108.6	95.2	83.6	73.4	
3.5	0.0	208.2	271.3	313.7	333.2	333.4	319.7	297.6	271.2	243.6	216.6	191.4	168.4	147.8	129.6	113.7	99.9	
4	0.0	0.0	354.3	409.7	435.2	435.4	417.6	388.7	354.2	318.2	282.9	249.9	219.9	193.0	169.3	148.6	130.5	
4.5	0.0	0.0	448.4	518.5	550.8	551.1	528.5	491.9	448.3	402.7	358.1	316.3	278.3	244.3	214.3	188.0	165.1	
5	0.0	0.0	0.0	640.2	680.1	680.4	652.5	607.3	553.5	497.2	442.1	390.5	343.6	301.6	264.6	232.1	203.8	
5.5	0.0	0.0	0.0	750.0	750.0	750.0	750.0	750.0	669.7	601.6	534.9	472.6	415.7	365.0	320.1	280.9	246.7	
6	0.0	0.0	0.0	0.0	750.0	750.0	750.0	750.0	750.0	750.0	636.6	562.4	494.8	434.3	381.0	334.3	293.5	
6.5	0.0	0.0	0.0	0.0	750.0	750.0	750.0	750.0	750.0	750.0	750.0	660.0	580.7	509.8	447.1	392.3	344.5	
7	0.0	0.0	0.0	0.0	0.0	750.0	750.0	750.0	750.0	750.0	750.0	750.0	750.0	591.2	518.6	455.0	399.5	
7.5	0.0	0.0	0.0	0.0	0.0	0.0	750.0	750.0	750.0	750.0	750.0	750.0	750.0	750.0	595.3	522.3	458.7	
8	0.0	0.0	0.0	0.0	0.0	0.0	0.0	750.0	750.0	750.0	750.0	750.0	750.0	750.0	750.0	594.2	521.8	
Hs																		

Figure 26: Power Matrix - Loss method 1

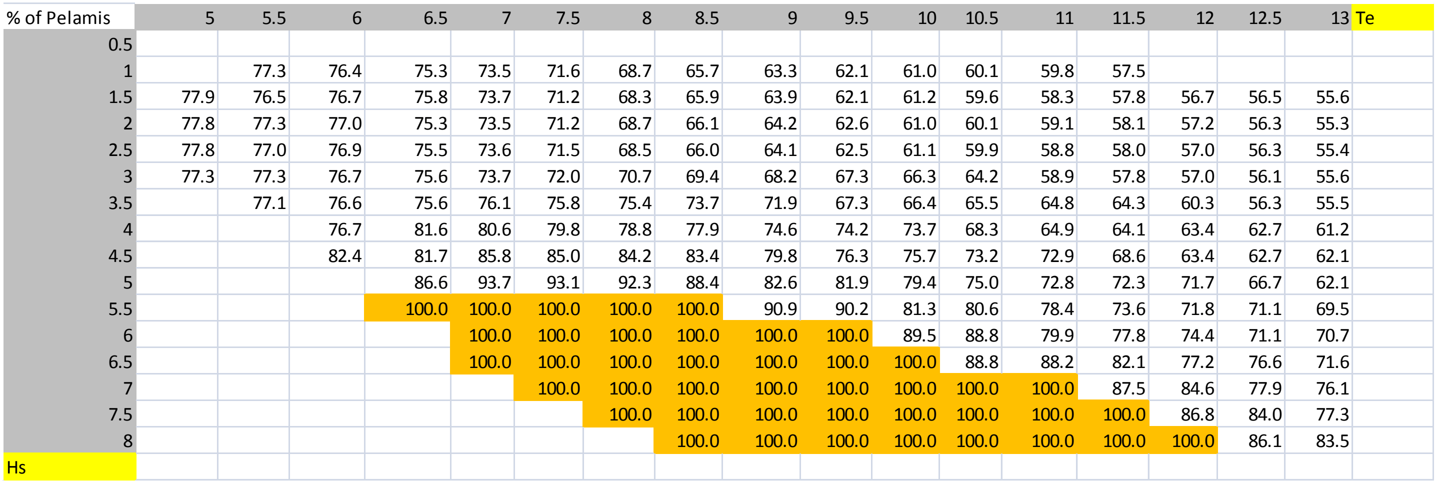

% of Pelamis	5	5.5	6	6.5	7	7.5	8	8.5	9	9.5	10	10.5	11	11.5	12	12.5	13	Te
0.5																		
1		77.3	76.4	75.3	73.5	71.6	68.7	65.7	63.3	62.1	61.0	60.1	59.8	57.5				
1.5	77.9	76.5	76.7	75.8	73.7	71.2	68.3	65.9	63.9	62.1	61.2	59.6	58.3	57.8	56.7	56.5	55.6	
2	77.8	77.3	77.0	75.3	73.5	71.2	68.7	66.1	64.2	62.6	61.0	60.1	59.1	58.1	57.2	56.3	55.3	
2.5	77.8	77.0	76.9	75.5	73.6	71.5	68.5	66.0	64.1	62.5	61.1	59.9	58.8	58.0	57.0	56.3	55.4	
3	77.3	77.3	76.7	75.6	73.7	72.0	70.7	69.4	68.2	67.3	66.3	64.2	58.9	57.8	57.0	56.1	55.6	
3.5		77.1	76.6	75.6	76.1	75.8	75.4	73.7	71.9	67.3	66.4	65.5	64.8	64.3	60.3	56.3	55.5	
4			76.7	81.6	80.6	79.8	78.8	77.9	74.6	74.2	73.7	68.3	64.9	64.1	63.4	62.7	61.2	
4.5			82.4	81.7	85.8	85.0	84.2	83.4	79.8	76.3	75.7	73.2	72.9	68.6	63.4	62.7	62.1	
5				86.6	93.7	93.1	92.3	88.4	82.6	81.9	79.4	75.0	72.8	72.3	71.7	66.7	62.1	
5.5				100.0	100.0	100.0	100.0	100.0	90.9	90.2	81.3	80.6	78.4	73.6	71.8	71.1	69.5	
6					100.0	100.0	100.0	100.0	100.0	100.0	89.5	88.8	79.9	77.8	74.4	71.1	70.7	
6.5					100.0	100.0	100.0	100.0	100.0	100.0	100.0	88.8	88.2	82.1	77.2	76.6	71.6	
7						100.0	100.0	100.0	100.0	100.0	100.0	100.0	100.0	87.5	84.6	77.9	76.1	
7.5							100.0	100.0	100.0	100.0	100.0	100.0	100.0	100.0	86.8	84.0	77.3	
8								100.0	100.0	100.0	100.0	100.0	100.0	100.0	100.0	86.1	83.5	
Hs																		

Figure 27: Percentage of Pelamis® Targeted Power Matrix - Loss method 1

When this is applied to the entire matrix, there is significant under estimation outside of the saturation zone. This is shown in Figure 27, where power at many of the higher periods is much lower than the targeted value.

2. Single value based on power output in North Atlantic Conditions

The second method considered is a loss ratio based on the yearly average power output for conditions in the North Atlantic. This is used because the design of the Pelamis® P1 is intended for North Atlantic conditions[10] where the machine has been tested. An occurrence matrix for the wave conditions in the North Atlantic is used to calculate the yearly average power output for both the targeted Pelamis® matrix and the calculated hydrodynamic matrix. This resulted in 497.9kW and 767.8kW, respectively. Giving a ratio of 1/1.54. This ratio is then applied to the entire matrix as done in method 1. But again, some of the values are significantly off, as seen in Figure 28.

% of Pelamis	5	5.5	6	6.5	7	7.5	8	8.5	9	9.5	10	10.5	11	11.5	12	12.5	13	Te
0.5																		
1		100.2	99.0	97.6	95.3	92.8	89.0	85.1	82.0	80.6	79.1	77.9	77.5	74.5				
1.5	101.0	99.2	99.4	98.3	95.6	92.3	88.5	85.4	82.8	80.6	79.4	77.2	75.6	74.9	73.5	73.2	72.1	
2	100.8	100.2	99.9	97.6	95.3	92.2	89.0	85.7	83.2	81.2	79.1	77.9	76.6	75.4	74.2	73.0	71.7	
2.5	100.9	99.8	99.7	97.9	95.4	92.7	88.9	85.6	83.1	81.0	79.2	77.7	76.3	75.2	73.9	73.0	71.8	
3	100.3	100.2	99.4	98.0	95.6	93.4	91.7	90.0	88.5	87.2	86.0	83.2	76.4	74.9	73.9	72.7	72.1	
3.5		100.0	99.3	98.0	98.6	98.2	97.8	95.5	93.3	87.2	86.1	85.0	83.9	83.3	78.2	73.0	71.9	
4			99.4	105.8	104.5	103.4	102.1	101.0	96.7	96.2	95.5	88.5	84.1	83.1	82.2	81.3	79.4	
4.5			106.9	105.9	111.2	110.3	109.1	108.1	103.4	98.9	98.1	94.9	94.5	89.0	82.2	81.2	80.5	
5				112.3	121.4	120.7	119.6	114.6	107.1	106.2	102.9	97.2	94.4	93.8	93.0	86.5	80.6	
5.5				129.6	129.6	129.6	129.6	129.6	117.8	116.9	105.4	104.5	101.7	95.4	93.1	92.2	90.1	
6					129.6	129.6	129.6	129.6	129.6	129.6	116.1	115.2	103.6	100.9	96.5	92.2	91.7	
6.5					129.6	129.6	129.6	129.6	129.6	129.6	129.6	115.2	114.4	106.4	100.1	99.3	92.9	
7						129.6	129.6	129.6	129.6	129.6	129.6	129.6	129.6	113.4	109.7	101.0	98.7	
7.5							129.6	129.6	129.6	129.6	129.6	129.6	129.6	129.6	112.5	108.9	100.3	
8								129.6	129.6	129.6	129.6	129.6	129.6	129.6	129.6	111.6	108.2	
Hs																		

Figure 28: Percentage of Pelamis® Targeted Power Matrix - Loss method 2

3. Matrix of values based on ratio from power output of occurrence matrix for each period

The third method does not use a single ratio applied to the entire matrix of conditions, but uses a matrix of ratios. These ratios are based on a period average of the published power matrix to the hydrodynamic calculated matrix. This gives a ratio for each period. Along with this, the saturation zone ratio is still maintained with the value from loss method 1. The ratios used are shown in Figure 29.

3.Period based coef.	5	5.5	6	6.5	7	7.5	8	8.5	9	9.5	10	10.5	11	11.5	12	12.5	13	Te
0.5	0	0	0	0	0	0	0	0	0	0	0	0	0	0	0	0	0	
1	0	1.5415	1.5643	1.6859	1.7906	1.8037	1.81614	1.8228	1.7849	1.7779	1.7406	1.7021	1.6762	1.6202	0	0	0	
1.5	1.5517	1.5415	1.5643	1.6859	1.7906	1.8037	1.81614	1.8228	1.7849	1.7779	1.7406	1.7021	1.6762	1.6202	1.552	1.4672	1.4139	
2	1.5517	1.5415	1.5643	1.6859	1.7906	1.8037	1.81614	1.8228	1.7849	1.7779	1.7406	1.7021	1.6762	1.6202	1.552	1.4672	1.4139	
2.5	1.5517	1.5415	1.5643	1.6859	1.7906	1.8037	1.81614	1.8228	1.7849	1.7779	1.7406	1.7021	1.6762	1.6202	1.552	1.4672	1.4139	
3	1.5517	1.5415	1.5643	1.6859	1.7906	1.8037	1.81614	1.8228	1.7849	1.7779	1.7406	1.7021	1.6762	1.6202	1.552	1.4672	1.4139	
3.5	0	1.5415	1.5643	1.6859	1.7906	1.8037	1.81614	1.8228	1.7849	1.7779	1.7406	1.7021	1.6762	1.6202	1.552	1.4672	1.4139	
4	0	0	1.5643	1.6859	1.7906	1.8037	1.81614	1.8228	1.7849	1.7779	1.7406	1.7021	1.6762	1.6202	1.552	1.4672	1.4139	
4.5	0	0	1.5643	1.6859	1.7906	1.8037	1.81614	1.8228	1.7849	1.7779	1.7406	1.7021	1.6762	1.6202	1.552	1.4672	1.4139	
5	0	0	0	1.6859	1.7906	1.8037	1.81614	1.8228	1.7849	1.7779	1.7406	1.7021	1.6762	1.6202	1.552	1.4672	1.4139	
5.5	0	0	0	1.9989	1.9989	1.9989	1.9989	1.9989	1.7849	1.7779	1.7406	1.7021	1.6762	1.6202	1.552	1.4672	1.4139	
6	0	0	0	0	1.9989	1.9989	1.9989	1.9989	1.9989	1.9989	1.7406	1.7021	1.6762	1.6202	1.552	1.4672	1.4139	
6.5	0	0	0	0	1.9989	1.9989	1.9989	1.9989	1.9989	1.9989	1.9989	1.7021	1.6762	1.6202	1.552	1.4672	1.4139	
7	0	0	0	0	0	1.9989	1.9989	1.9989	1.9989	1.9989	1.9989	1.9989	1.9989	1.6202	1.552	1.4672	1.4139	
7.5	0	0	0	0	0	0	1.9989	1.9989	1.9989	1.9989	1.9989	1.9989	1.9989	1.9989	1.552	1.4672	1.4139	
8	0	0	0	0	0	0	0	1.9989	1.9989	1.9989	1.9989	1.9989	1.9989	1.9989	1.999	1.4672	1.4139	
Hs																		

Figure 29: Method 3 - Period Based Loss Coefficient Matrix

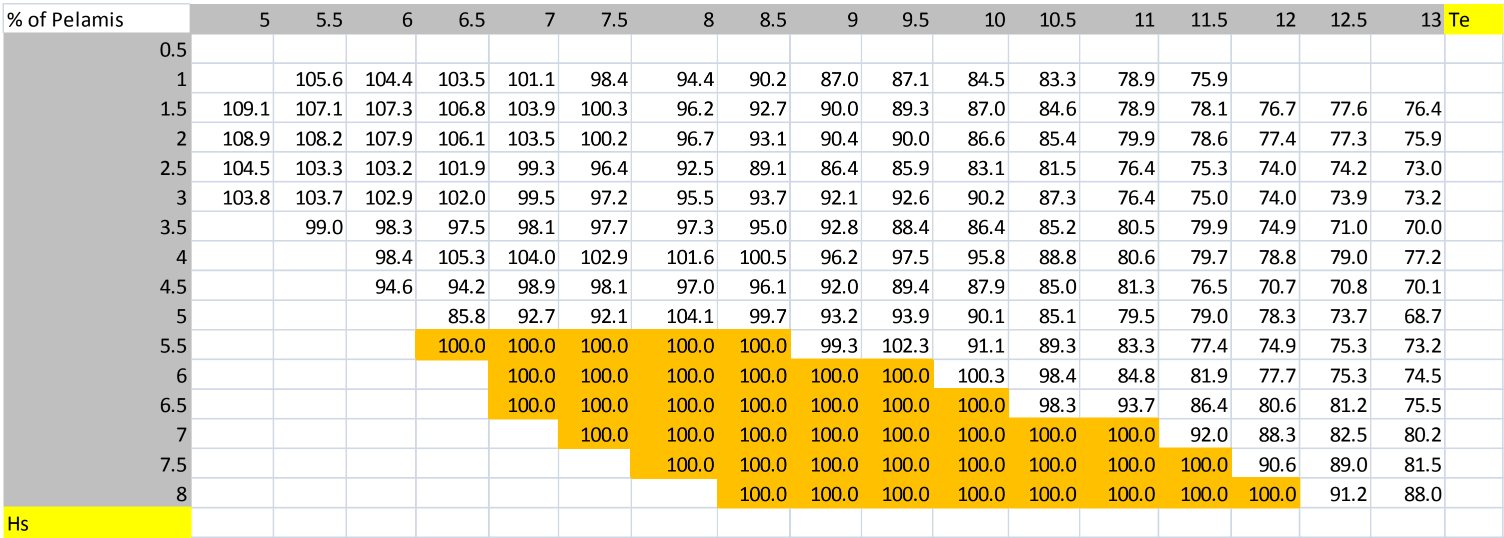

% of Pelamis	5	5.5	6	6.5	7	7.5	8	8.5	9	9.5	10	10.5	11	11.5	12	12.5	13	Te
0.5																		
1		105.6	104.4	103.5	101.1	98.4	94.4	90.2	87.0	87.1	84.5	83.3	78.9	75.9				
1.5	109.1	107.1	107.3	106.8	103.9	100.3	96.2	92.7	90.0	89.3	87.0	84.6	78.9	78.1	76.7	77.6	76.4	
2	108.9	108.2	107.9	106.1	103.5	100.2	96.7	93.1	90.4	90.0	86.6	85.4	79.9	78.6	77.4	77.3	75.9	
2.5	104.5	103.3	103.2	101.9	99.3	96.4	92.5	89.1	86.4	85.9	83.1	81.5	76.4	75.3	74.0	74.2	73.0	
3	103.8	103.7	102.9	102.0	99.5	97.2	95.5	93.7	92.1	92.6	90.2	87.3	76.4	75.0	74.0	73.9	73.2	
3.5		99.0	98.3	97.5	98.1	97.7	97.3	95.0	92.8	88.4	86.4	85.2	80.5	79.9	74.9	71.0	70.0	
4			98.4	105.3	104.0	102.9	101.6	100.5	96.2	97.5	95.8	88.8	80.6	79.7	78.8	79.0	77.2	
4.5			94.6	94.2	98.9	98.1	97.0	96.1	92.0	89.4	87.9	85.0	81.3	76.5	70.7	70.8	70.1	
5				85.8	92.7	92.1	104.1	99.7	93.2	93.9	90.1	85.1	79.5	79.0	78.3	73.7	68.7	
5.5				100.0	100.0	100.0	100.0	100.0	99.3	102.3	91.1	89.3	83.3	77.4	74.9	75.3	73.2	
6					100.0	100.0	100.0	100.0	100.0	100.0	100.3	98.4	84.8	81.9	77.7	75.3	74.5	
6.5					100.0	100.0	100.0	100.0	100.0	100.0	100.0	98.3	93.7	86.4	80.6	81.2	75.5	
7						100.0	100.0	100.0	100.0	100.0	100.0	100.0	100.0	92.0	88.3	82.5	80.2	
7.5							100.0	100.0	100.0	100.0	100.0	100.0	100.0	100.0	90.6	89.0	81.5	
8								100.0	100.0	100.0	100.0	100.0	100.0	100.0	100.0	91.2	88.0	
Hs																		

Figure 30: Percentage of Pelamis® Targeted Power Matrix - Loss method 3

The percentage of the Method 3 power matrix to the Pelamis® targeted power matrix is shown in Figure 30. There is some error but overall, it seems to yield a better approximation of the loss than Method 1 or 2. This period-based coefficient loss method will be used for the remainder of study in order to estimate yearly average power. It is applied to the single and multiple machine power calculations in order to approximate losses.

9. Multiple machines

Multiple machines can be looked at easily in WAMIT™ using the same basic input files as for the single machine. The same .frc file with Mass and Damping matrix can be called upon for each machine, while the .pot file defines origin and position of the local coordinate system for each body. Along with this, the same .gdf file (mesh) is called upon for each body. The configuration file needs to be adjusted for the number of CPUs and RAM used because with an increase in body numbers N, there is a significant increase in the number of equations solved. In addition to the changes in the input files, the internal .dll file for the added hinge modes is rewritten to include multiple bodies each with added modes.

To first confirm that the multiple machine runs are estimating as intended, a few tests are run. The first tests include two machines (N=2) located at varying distances side by side shown in Figure 31 and Figure 35. In these tests, both machines see head waves.

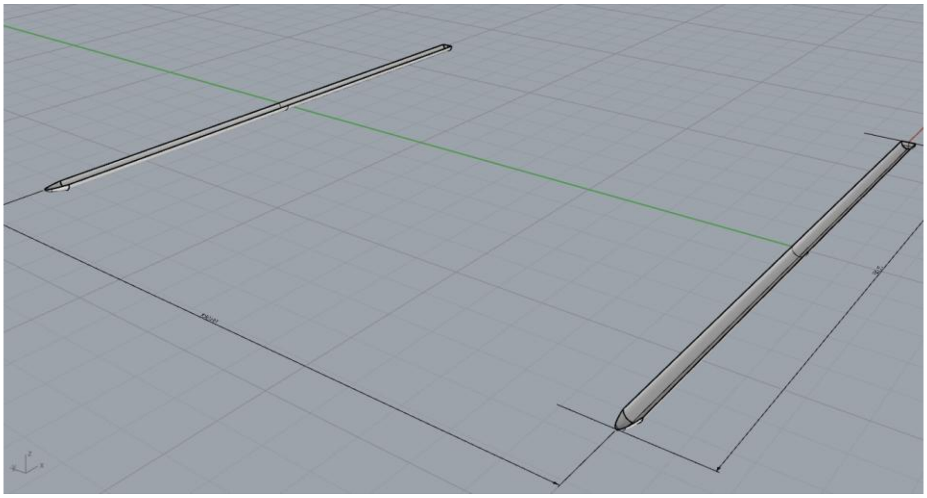

Figure 31: Two Machines Side by Side - 150m apart

The first separation distance, 150m, should yield RAOs essentially identical to each other as well as to the single machine's. This is inferred with such a large distance because no interaction is expected between the machines. The following plots show the angular RAOs at each hinge for the two machines and for a single machine:

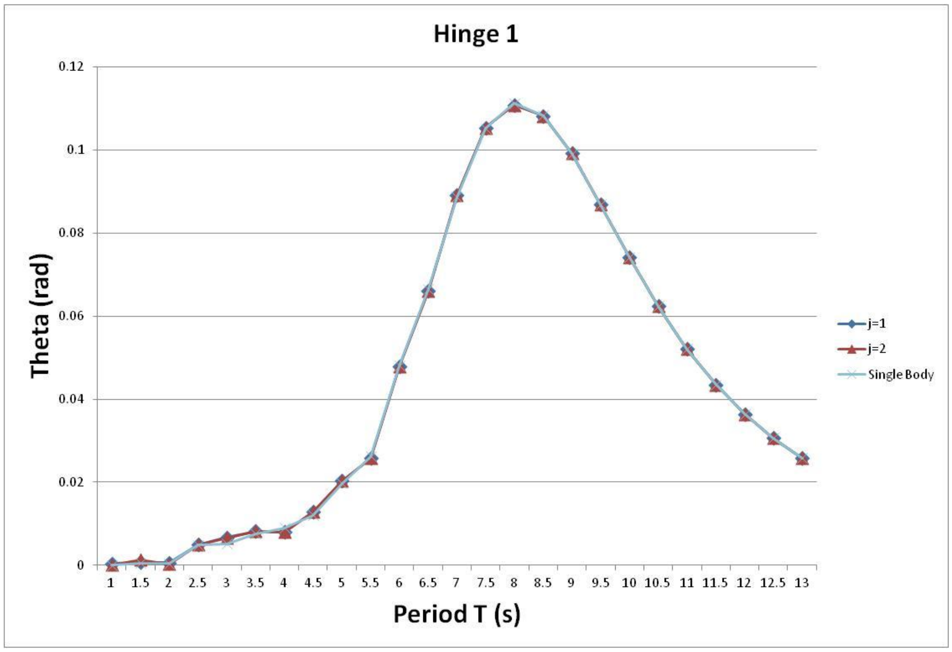

Figure 32: Two machines (150m - side) RAO - Hinge 1

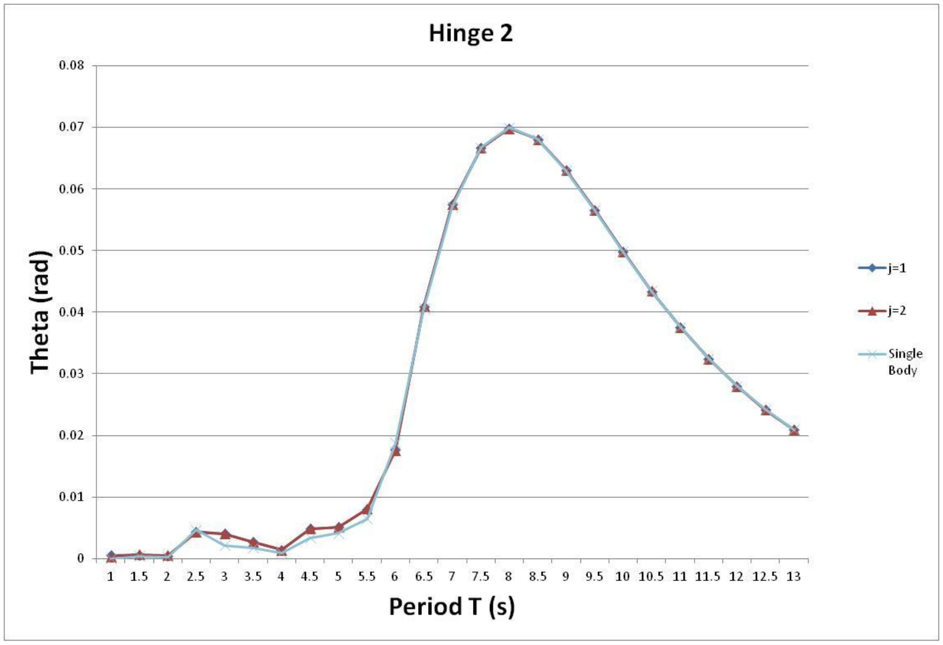

Figure 33: Two machines (150m - side) RAO - Hinge 2

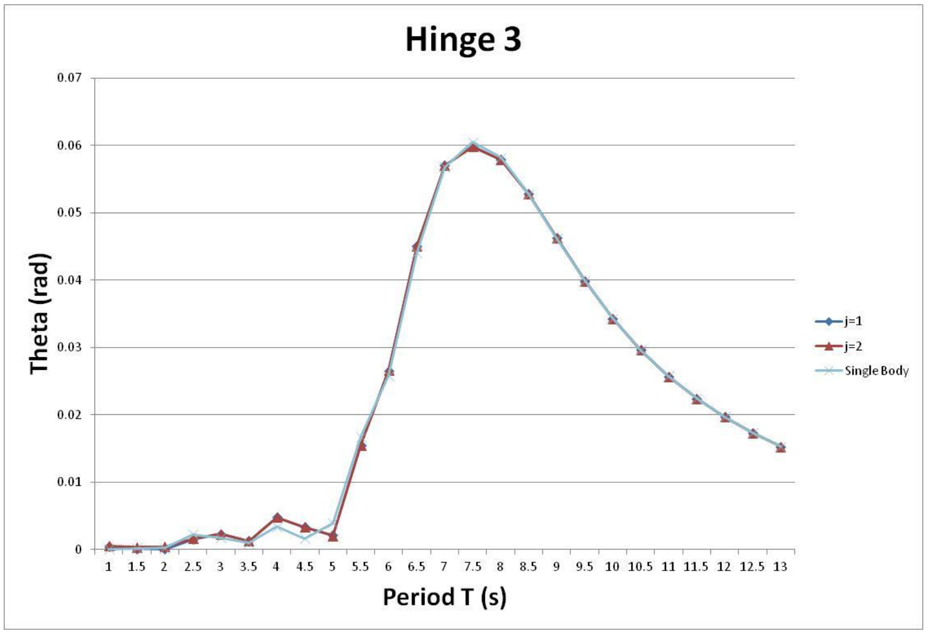

Figure 34: Two machines (150m - side) RAO - Hinge 3

The next test uses the much smaller distance of 10m in an effort to show a change in the motion RAOs.

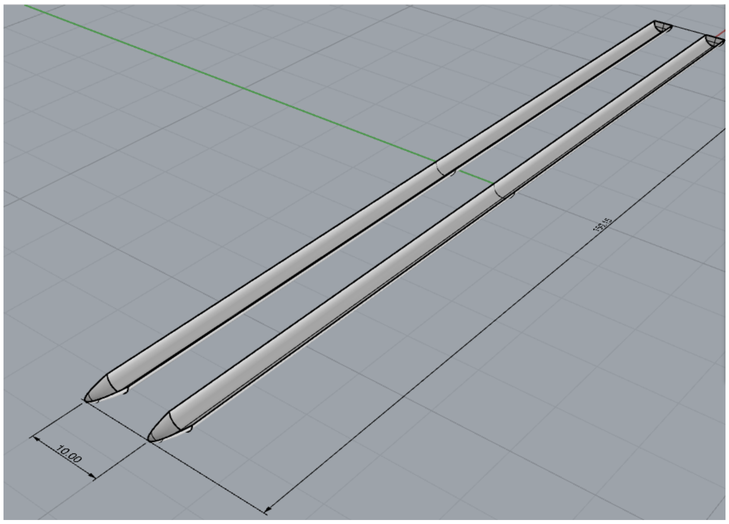

Figure 35: Two Machines Side by Side - 10m apart

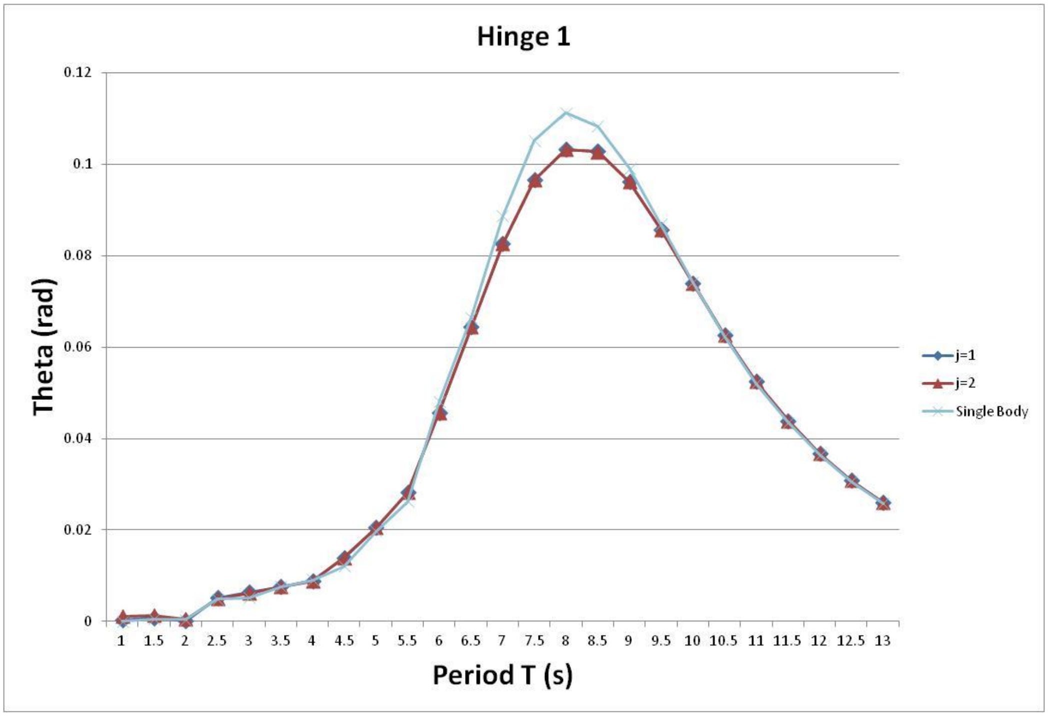

Figure 36:Two machines (10m - side) RAO - Hinge 1

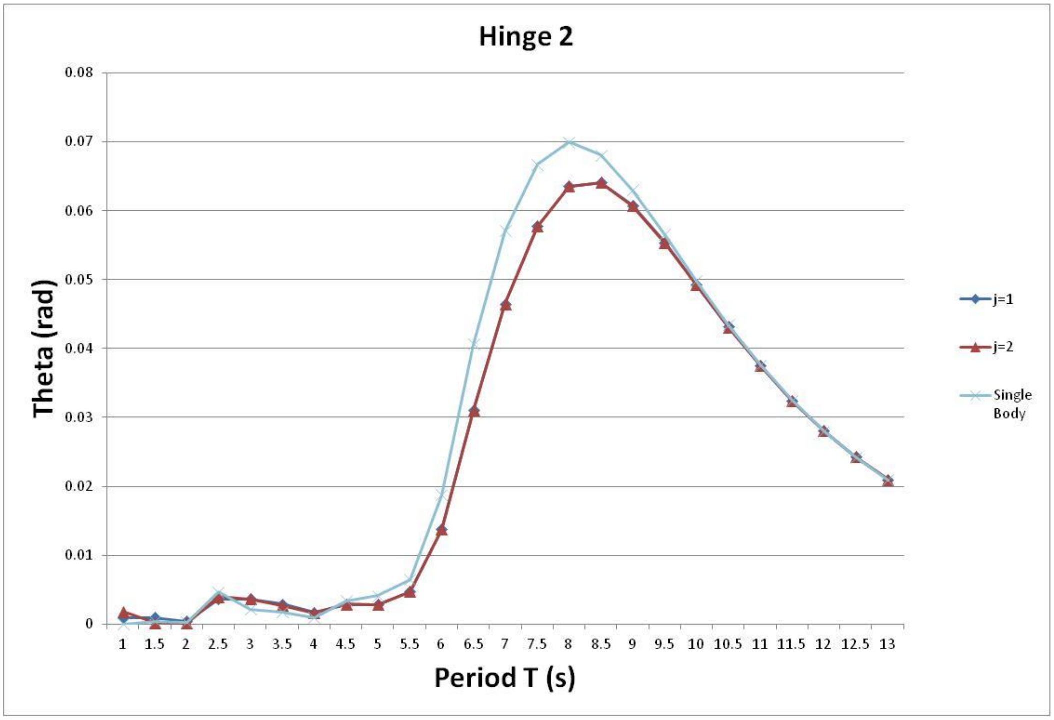

Figure 37: Two machines (10m - side) RAO - Hinge 2

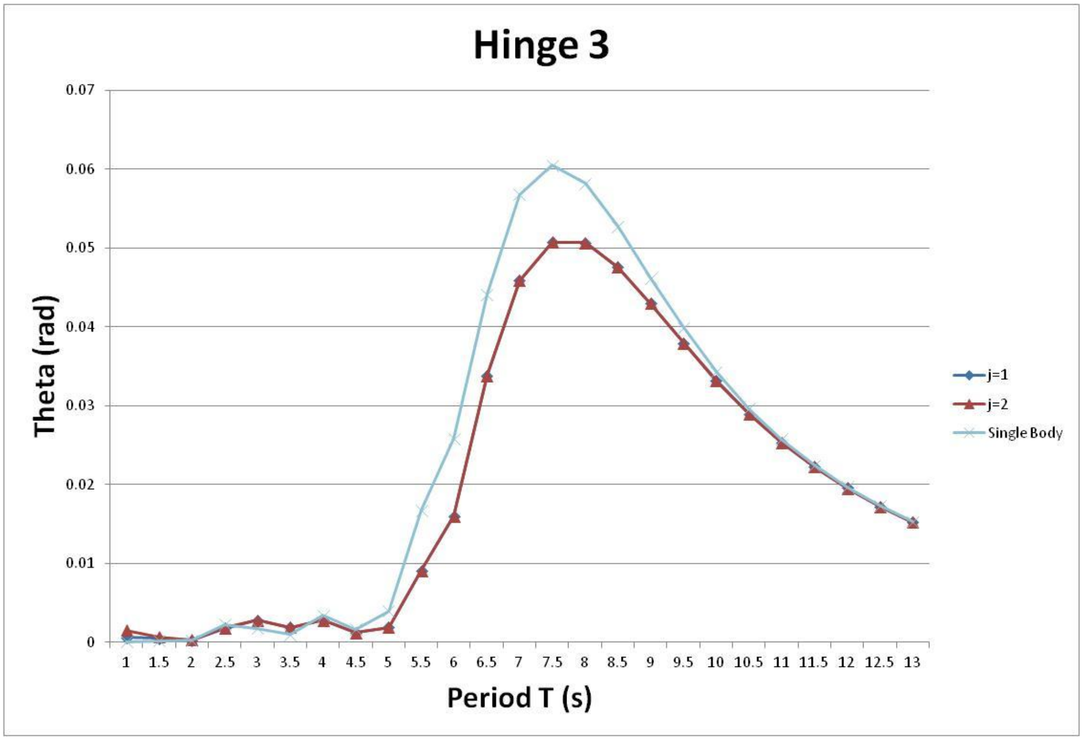

Figure 38: Two machines (10m - side) RAO - Hinge 3

The RAO plots in Figure 36,Figure 37 andFigure 38 show destructive interference between the two machines. Both bodies j=1 and j=2 show decreased motion but similar trends to those of the single body.

Next the machines are lined up nose to tail in order to see loss of motion of the trailing machine as shown in Figure 39.

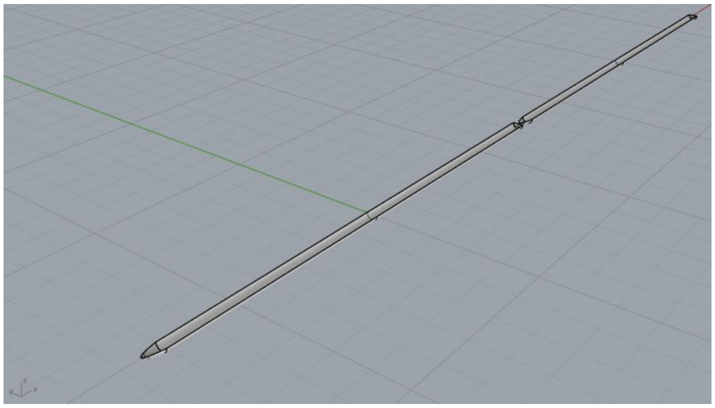

Figure 39: Two Machines Nose to Tail - 0m apart

This arrangement should see a decrease in motion for body 2, which is directly behind body 1 in head waves. This is confirmed in Figure 40, Figure 41 andFigure 42.

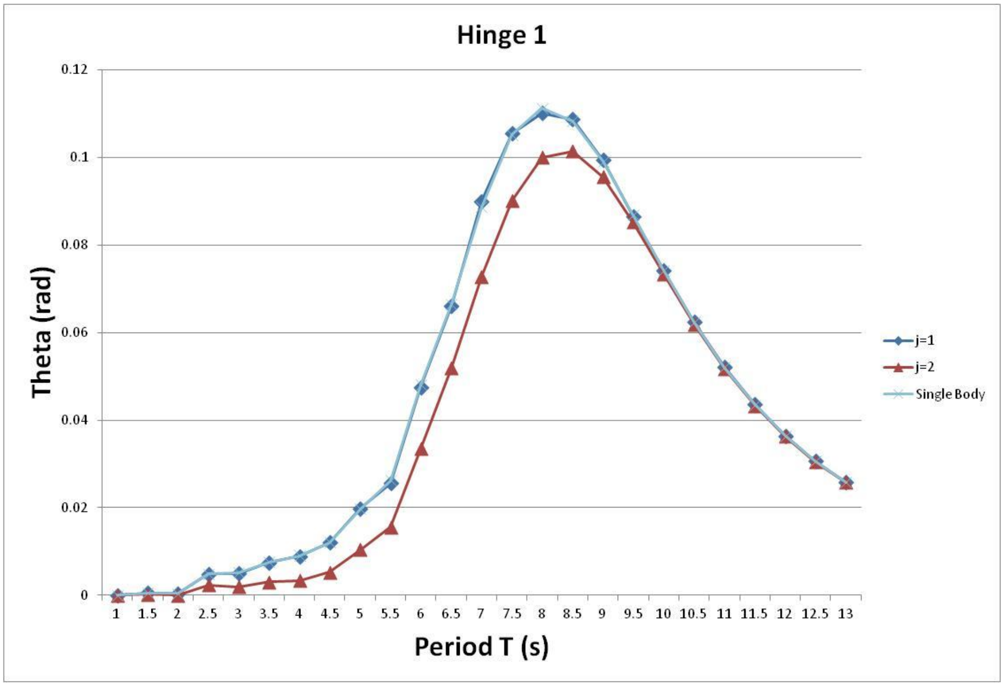

Figure 40: Two machines (0m - nose to tail) RAO - Hinge 1

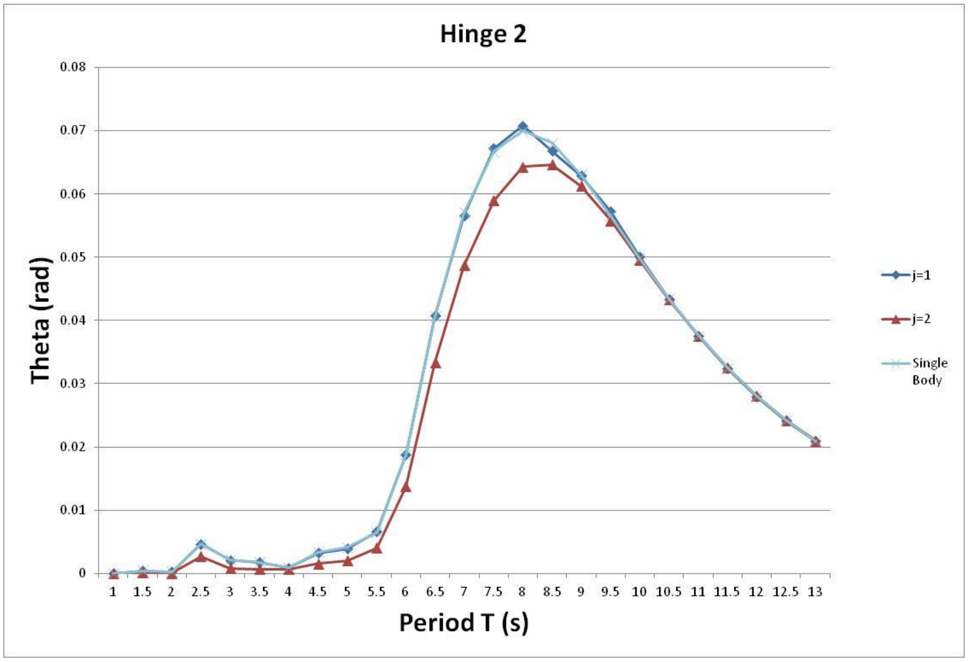

Figure 41: Two machines (0m - nose to tail) RAO - Hinge 2

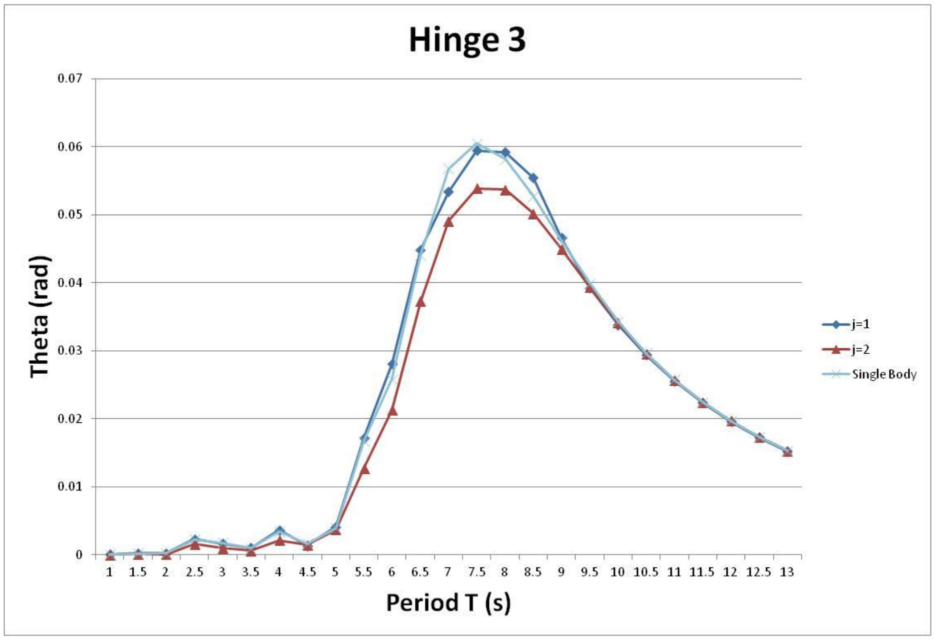

Figure 42: Two machines (0m - nose to tail) RAO - Hinge 3

The next set up uses a larger spacing for the nose to tail formation.

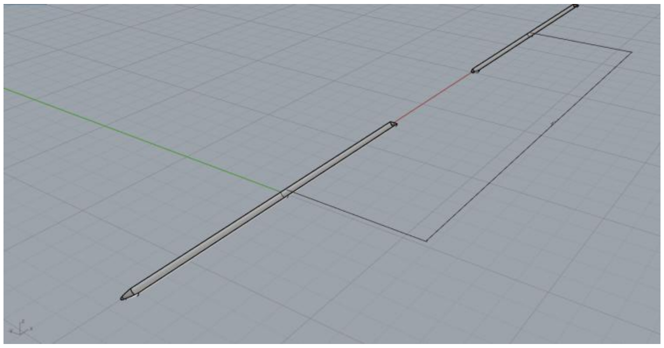

Figure 43: Two Machines Nose to Tail - 75m apart

This should result in a decrease in motion of the hinges of the down-wave body j=2, but not as significantly as in the previous test with 0m spacing.

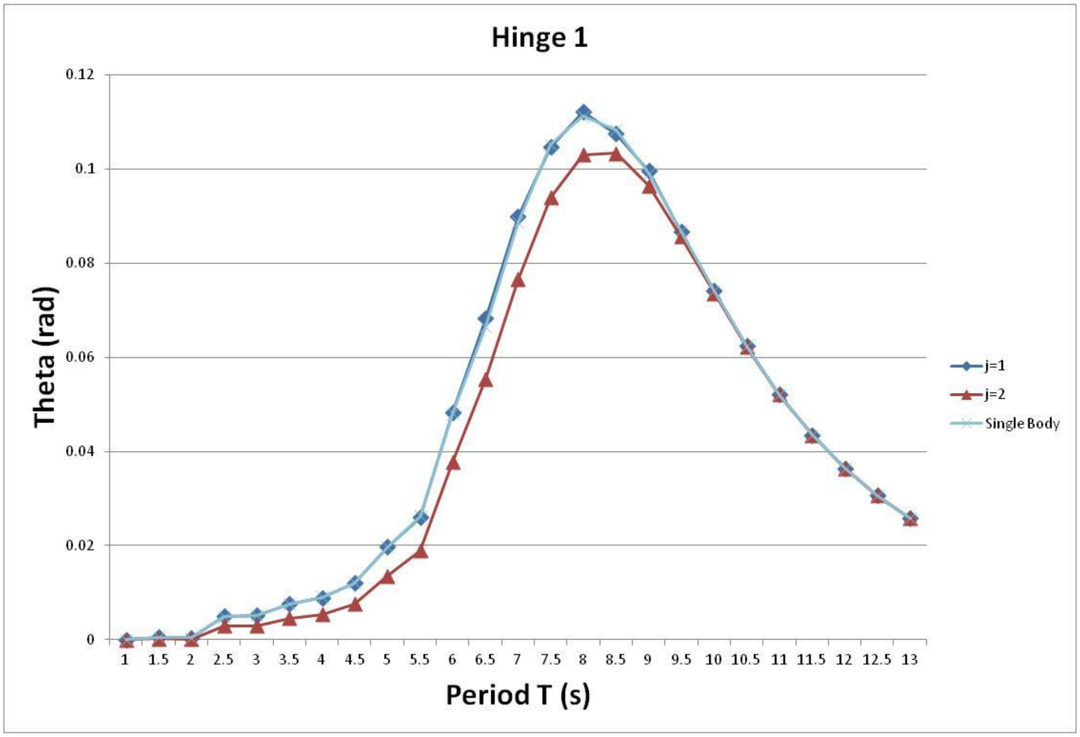

Figure 44: Two machines (75m - nose to tail) RAO - Hinge 1

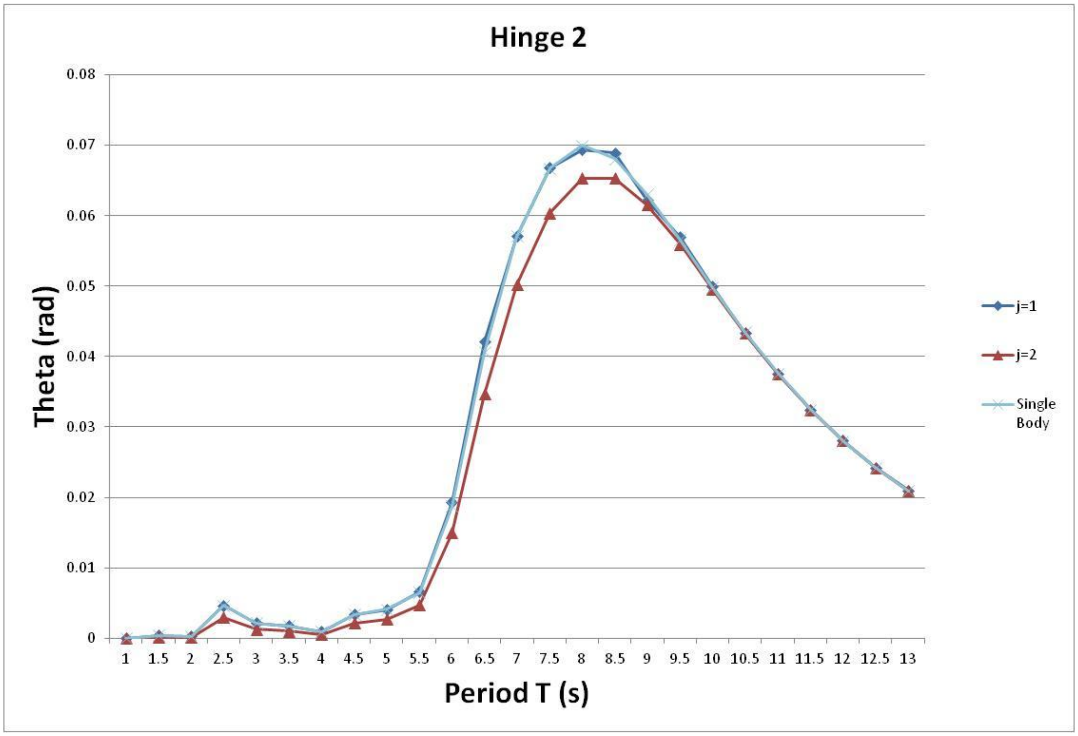

Figure 45: Two machines (75m - nose to tail) RAO - Hinge 2

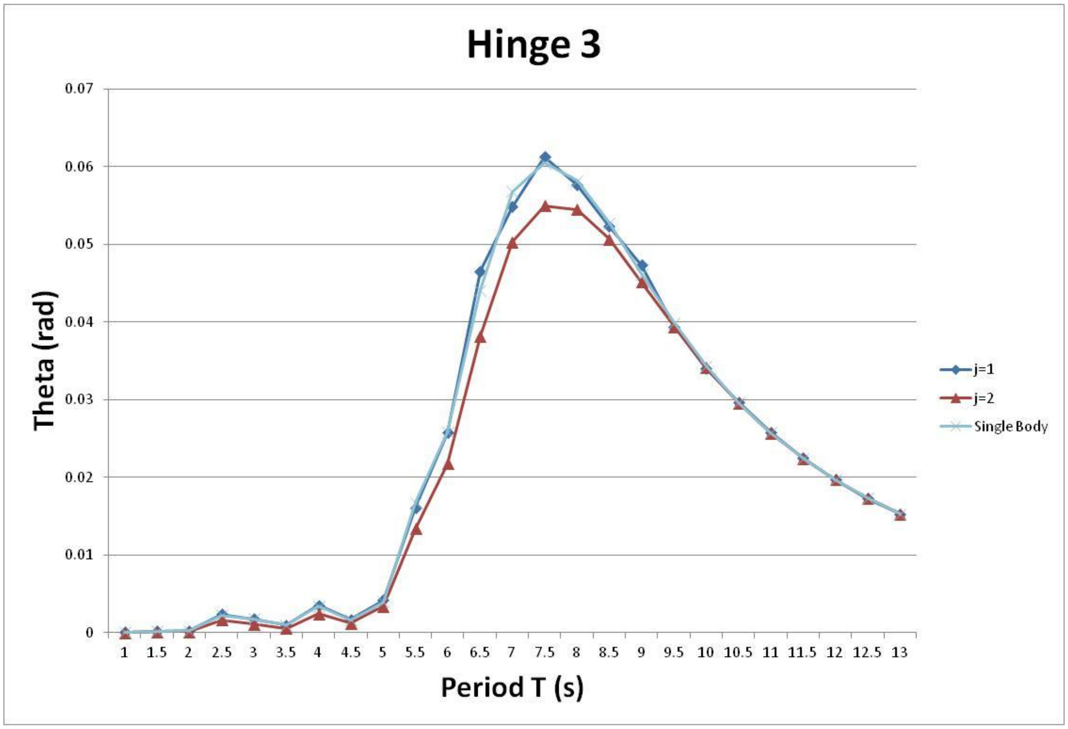

Figure 46: Two machines (75m - nose to tail) RAO - Hinge 3

Figure 44, Figure 45 andFigure 46 show the decrease in angular motion of hinges for body j=2 but not as much as with 0m spacing. Hinge 1 shows close motions for j=1 and j=2. Even with such small differences in the RAO, a larger difference in power output will occur. This is because the power output is proportional to the square of the motion RAO as seen in Equation 6.8.

With the preliminary tests simply confirming machine interaction, a larger number of machines can be considered (N>2). The set up for this larger number of machines is based on a checkerboard pattern with row (s_R) and column (s_C) spacing shown in Figure 6. These spacing increments are a factor of the overall machine length L =150m. Starting out with the recommended spacing of L x .5L (s_C x s_R) given in the Pelamis® Manual[3], it is then increased and decreased in size in order to see the constructive and destructive effects at different spacing distances. Initial checkerboard configurations are (s_C x s_R):

- 4L x L
- 2L x L
- L x .5L
- .5L x .25L
- .25L, .125L

This is done for 10, 15 and 18 machines for validation, with 15 and 18 unit configurations having 3 rows of machines and the 10 machine set up only having 2 rows. In order to compare all the data, a power factor Q is defined:

$$Q = \frac{\sum_{j=1}^{n} P_{calc}}{P_{single} * n} \tag{9.1}$$

where:

P_{calc}= Yearly average power output of machine j, in multiple machine set up in North Atlantic conditions

P_{Single}= Yearly average power output for single machine in North Atlantic conditions

n = Number of machines in selected group

Q can be defined for a single machine (n=1), a whole row(Q_{ROW}) where n=n_{ROW} or for the entire field of machines (Q_{TOT}) with n=N. This value is a good index to quantify constructive and destructive interference effects in a straightforward manner. This can be seen in the results from a 21 machine run in Figure 47.

10. Results

				Q_TOT	0.98325									
	1			1.007912										
		|												
------>		L			<--.5L-->		8		0.965257					
		|												
	2			1.01294							14			0.933128
------>							9		0.975197					
	3			1.016181							15			0.962568
------>							10		0.982155					
	4			1.020745							16			0.96749
------>							11		0.98233					
	5			1.015929							17			0.963333
------>							12		0.975512					
	6			1.013362							18			0.933148
------>							13		0.965447					
	7			1.005855										
------>								%drop	3.844804					6.053791

Figure 47: 18 Machines - L x .5L - Q output

Shown above in Figure 47 is an 18 machine configuration with an L x .5L spacing and incoming waves from the left. Each body in red is labeled with the body number j(1-18) as well as the individual Q for that machine. At the top of the figure is the overall Q_{TOT} and at the bottom is the percentage drop in yearly average power output for the 2nd and 3rd rows relative to the 1st. As the spacing gets larger, Q for each machine should tend to 1, as there is less and less interference. Along with this, the closer the spacing becomes, the smaller Q will become for most machines. Looking at Figure 47, there is consistency in row production as well as expected symmetry across the middle of the field parallel to the direction of the wave heading.

In order to further assess machine interference for variable spacing, the averaged row output, Q_{ROW}, is plotted for many configurations in Figure 48, which shows the spacing and overall machine number on the far right (N). The bracketed plot lines have the same spacing but a different number of machines, and in the 10 machine case, only 2 rows.

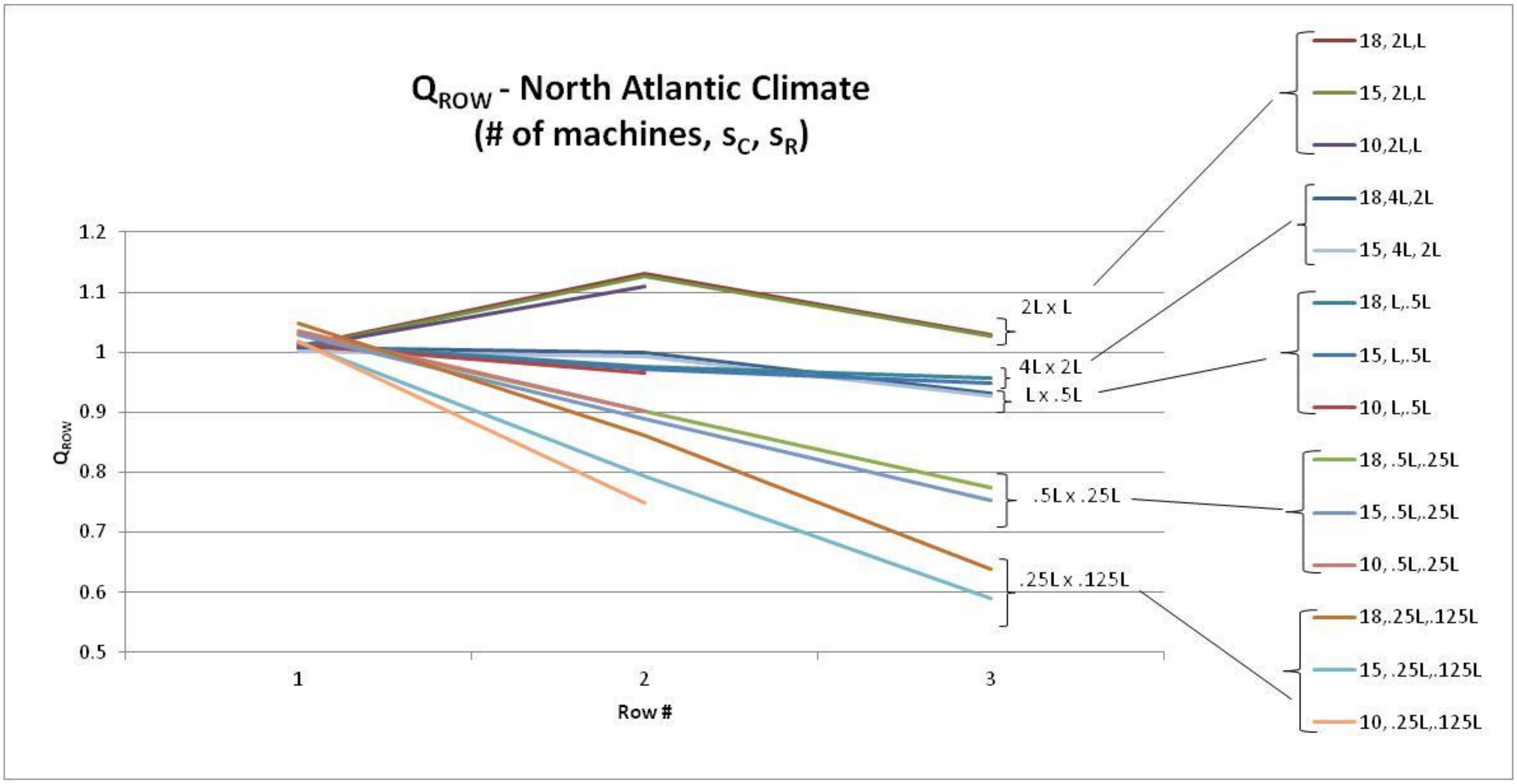

Figure 48: Q_{ROW} Varying Spacing and Machine number

Another way to look at this data is to assess power loss percentage on each row. This is shown in Figure 49.

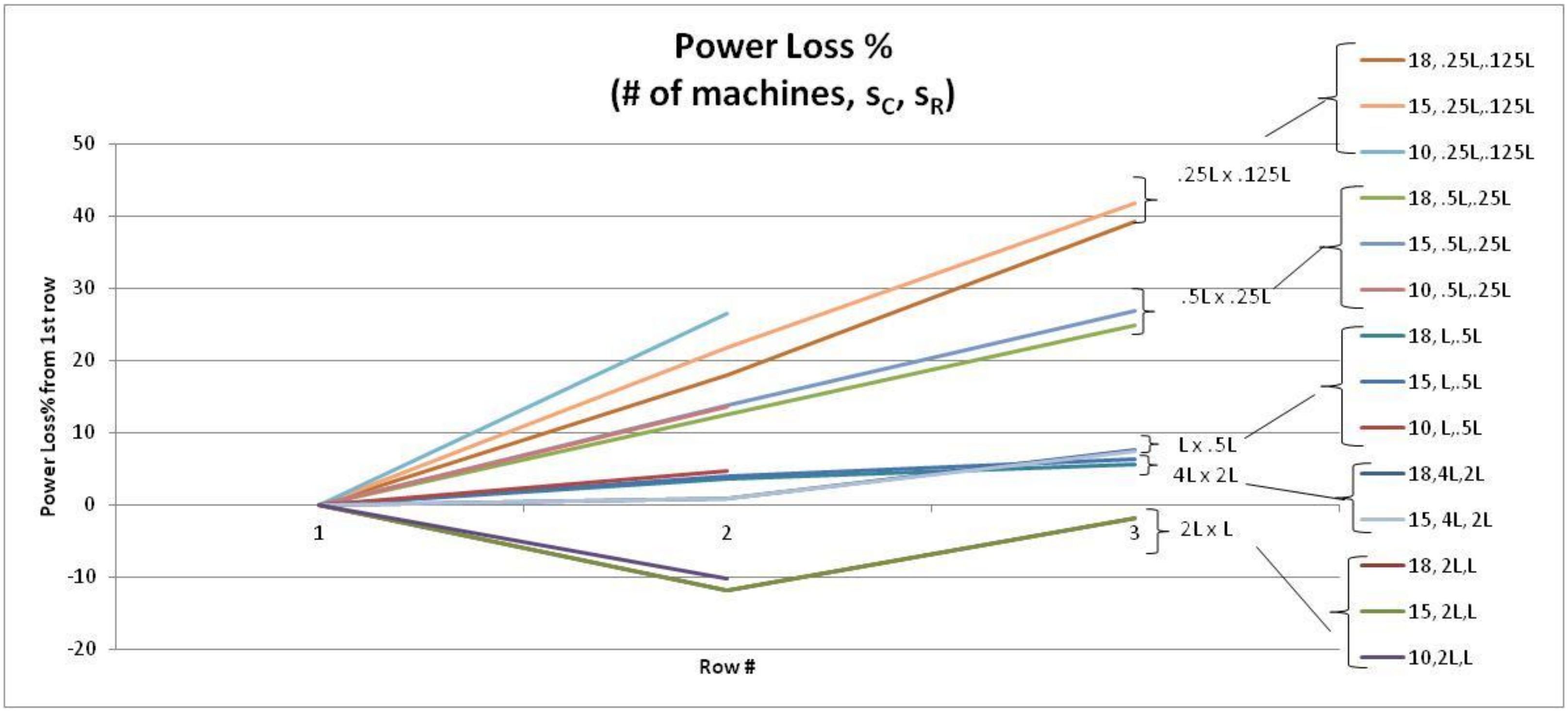

Figure 49: Power Loss %

The 2L x L spacing does not follow the trend of destructive interference in subsequent rows. The trend for other spacings shows a larger power loss as the bodies get closer together. This peculiar increase in yearly average power production can be explained with constructive interference, a phenomenon in which the spacing allows for waves in the 2nd and 3rd row to see an amplification of the incoming wave height. This is ideal in order to achieve the most efficient set up. Individual RAOs must be investigated to confirm that the motion of the bodies has increased. Shown in Figure 50, 51 and Figure 52 are the RAOs for hinge 1, 2 and 3 respectively. The line style indicates row location while the color shows the respective body index number, j. The motion RAOs of a single machine are also shown for comparison.

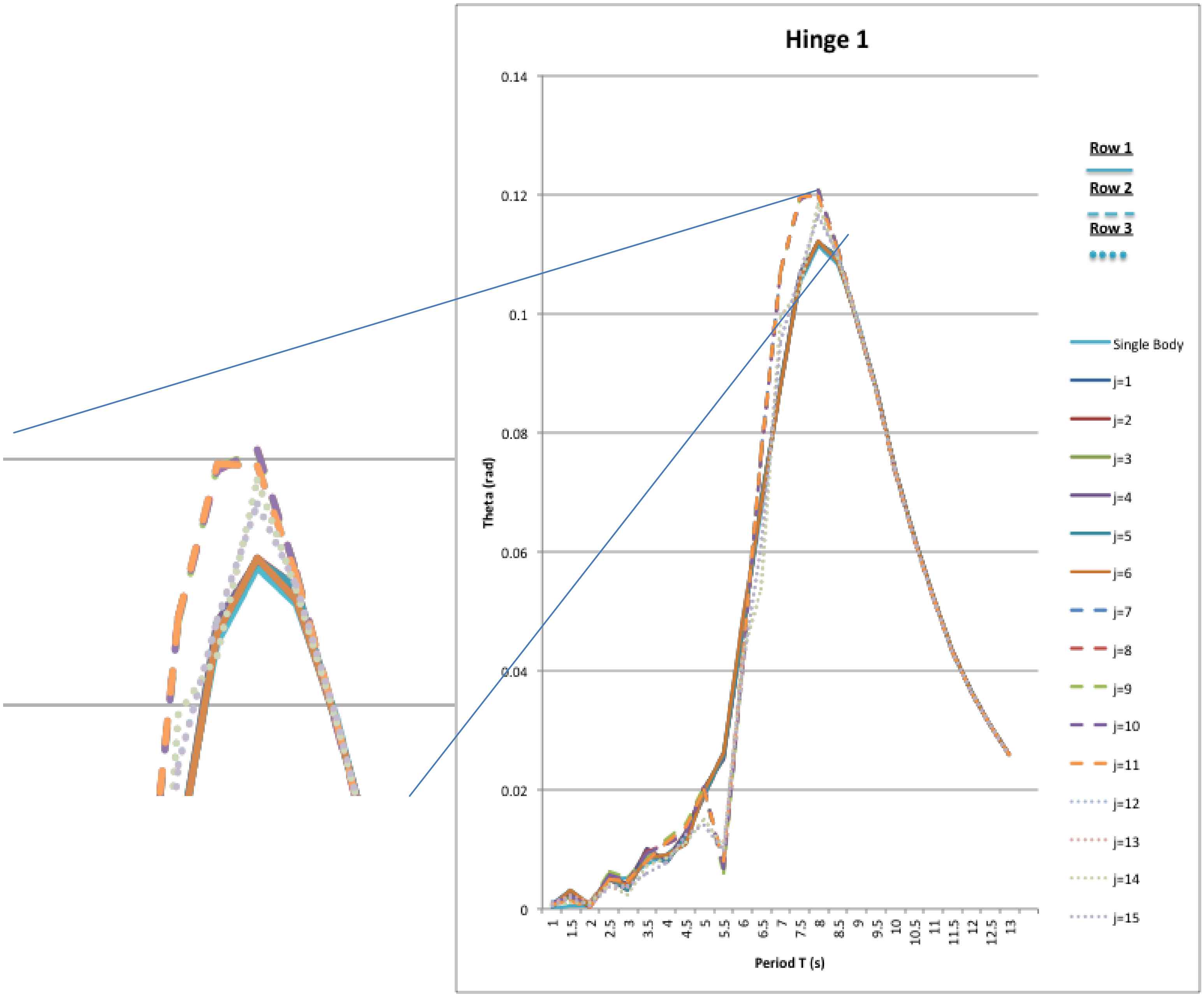

Figure 50: RAO (rad) of Hinge 1, 15 bodies, 2L x L

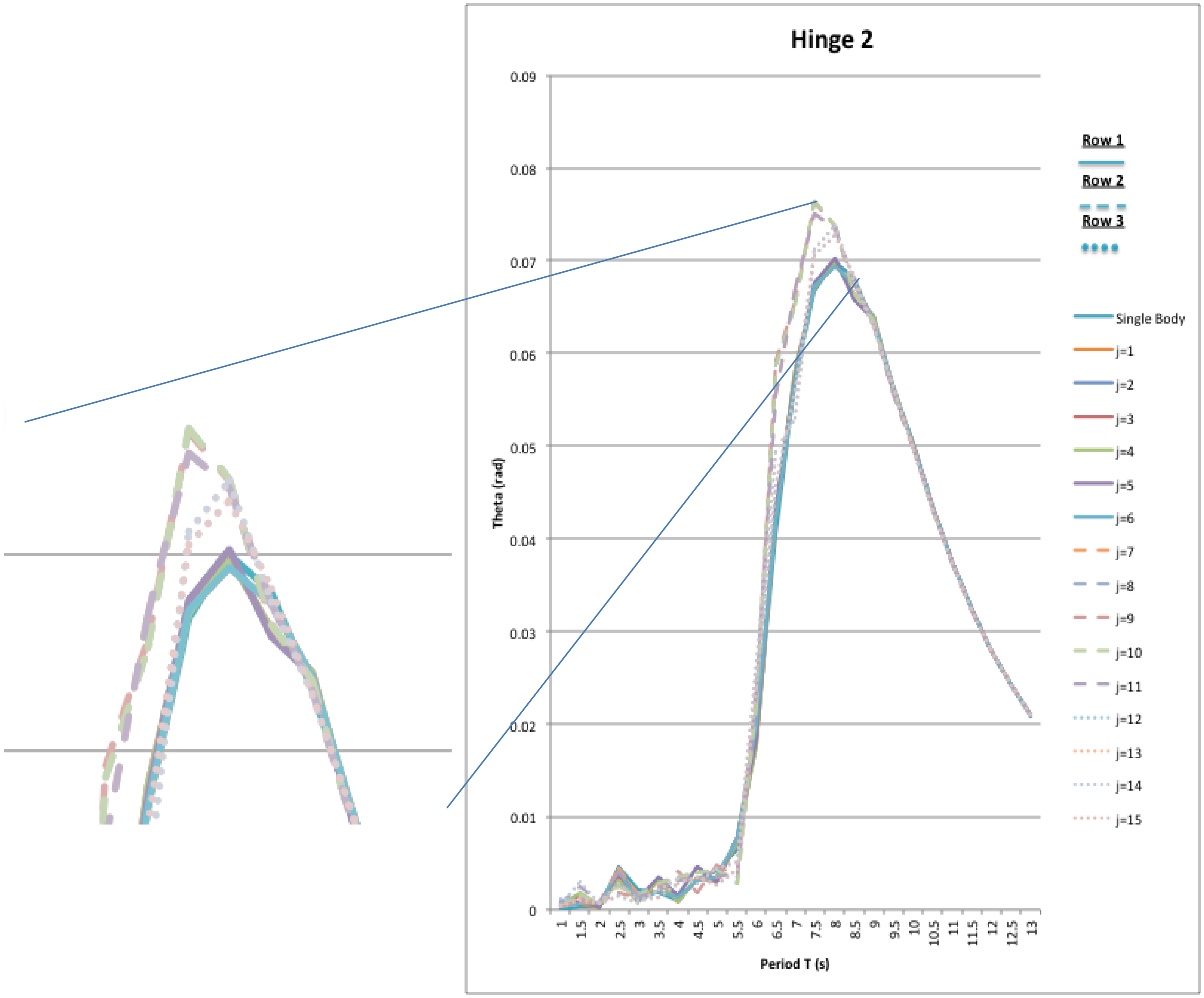

Figure 51: RAO (rad) of Hinge 2, 15 bodies, 2L x L

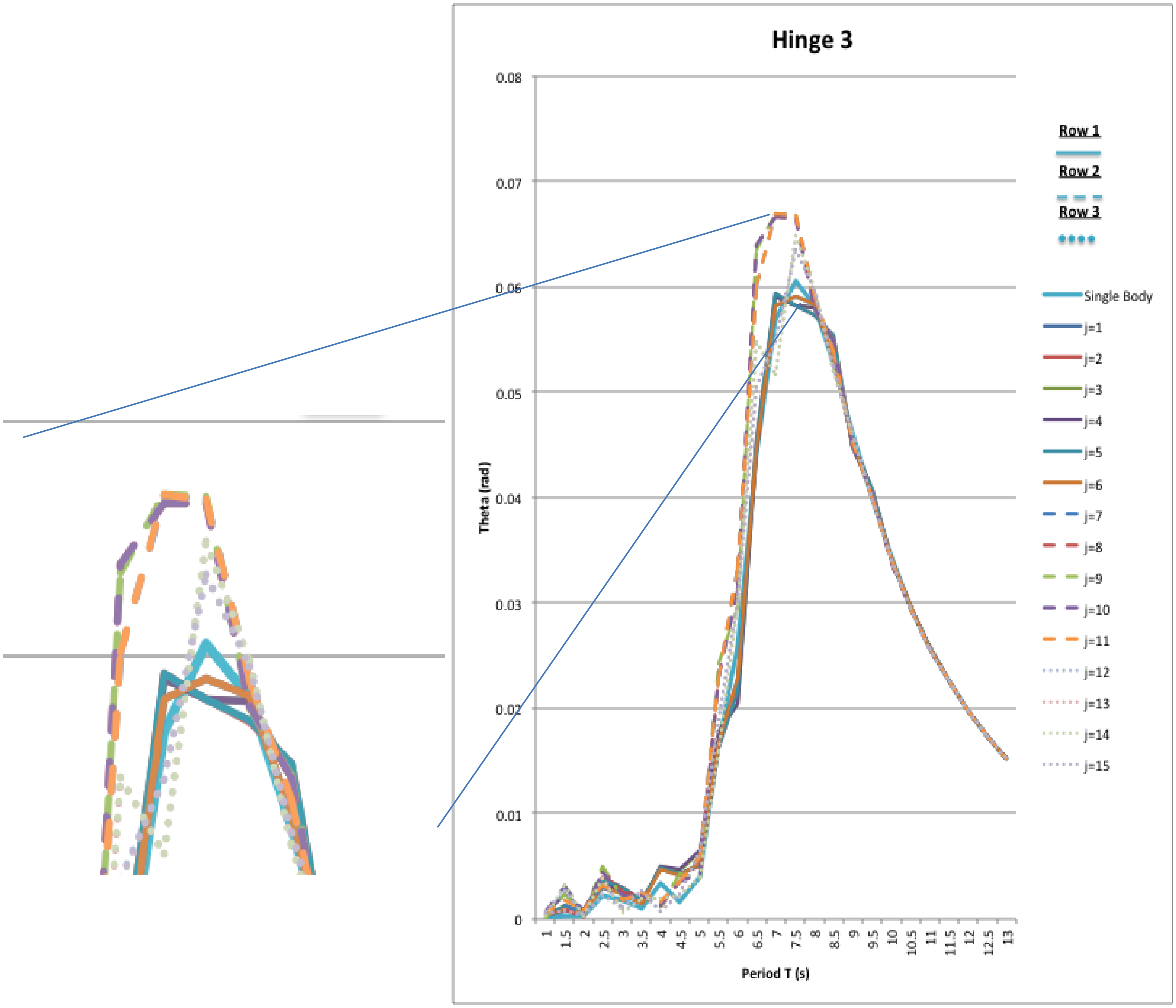

Figure 52: RAO (rad) of Hinge 3, 15 bodies, 2L x L

The large motions at periods from 5.5 to 10s correspond to high production conditions in the power matrix. All three hinges see an increase in motion for the 2nd row relative to the first row and the single machine. This occurs at the peak of motion (≈7.5-8s). This would correspond to the increase in Q at subsequent rows for this set up.

Since this set up will constructively interfere, tests will be run in order to find a possible maximum. Because power drop and Q trends hold for a varying number of machines in the same spacing set up, a small number of machines are used here in order to reduce computer run times.

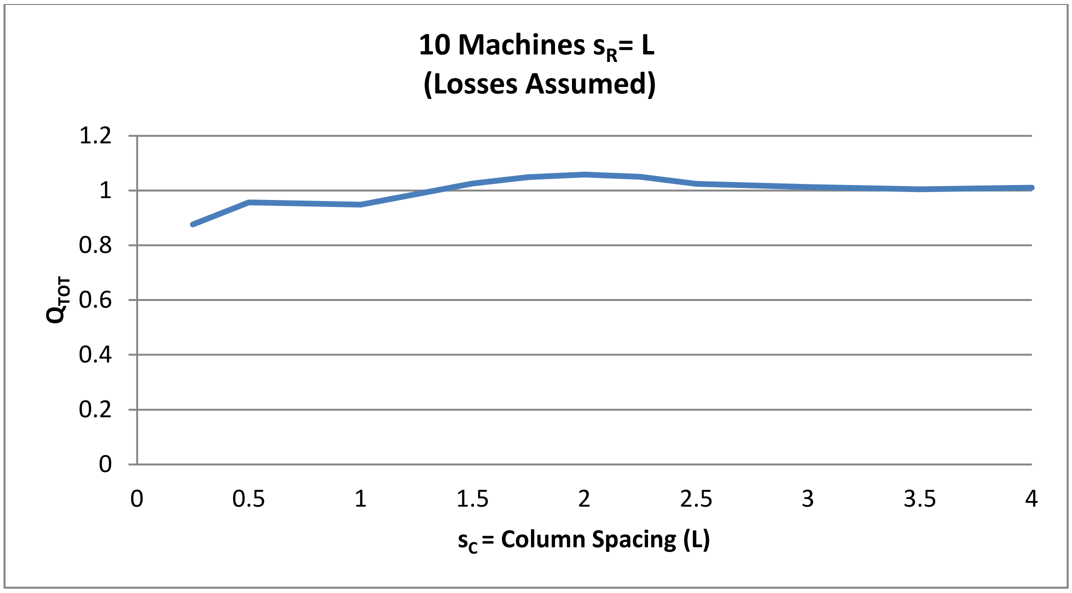

Figure 53: Q of 10 machines constant row spacing = L

Shown in Figure 53 is Q_{TOT} for 10 machine runs at a constant row spacing L with variable column spacing. There is a slight peak at a column spacing of 2L. From there, the increase in spacing causes Q_{TOT} to trend toward 1, as expected. With this information, the length of 2 L for column spacing is held constant while the row spacing is varied.

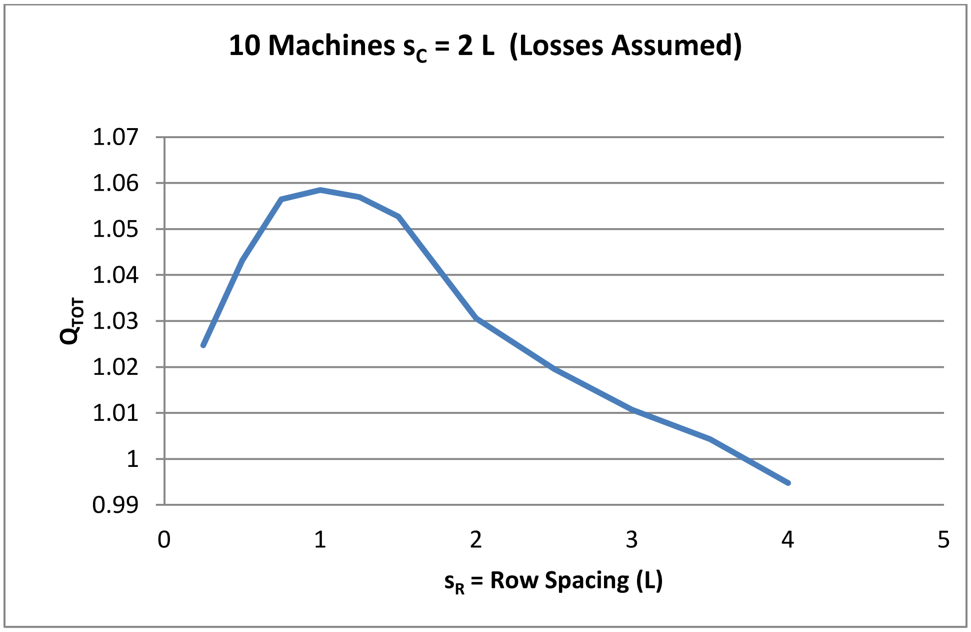

Figure 54: Q of 10 machines constant column spacing =2L

Shown in Figure 54 is Q_{TOT}, with a notable peak that decrease as the spacing gets larger. The dimensions S_C=2L and S_R=L are kept due to peak in Q_{TOT} and small area for WEC farm. A smaller farm area is less constrictive on waterways for boating and shipping traffic.

Another method used to see the amplification in Q and subsequent hinge motions is by looking at field point water elevation around the bodies. This option is available in WAMIT™ by inputting a field of points in the flow field. Generating an optional output, WAMIT™ will calculate the Pressure/Free surface elevation at these points. This can be expressed as a Wave Amplitude Ratio, based on incoming wave size.

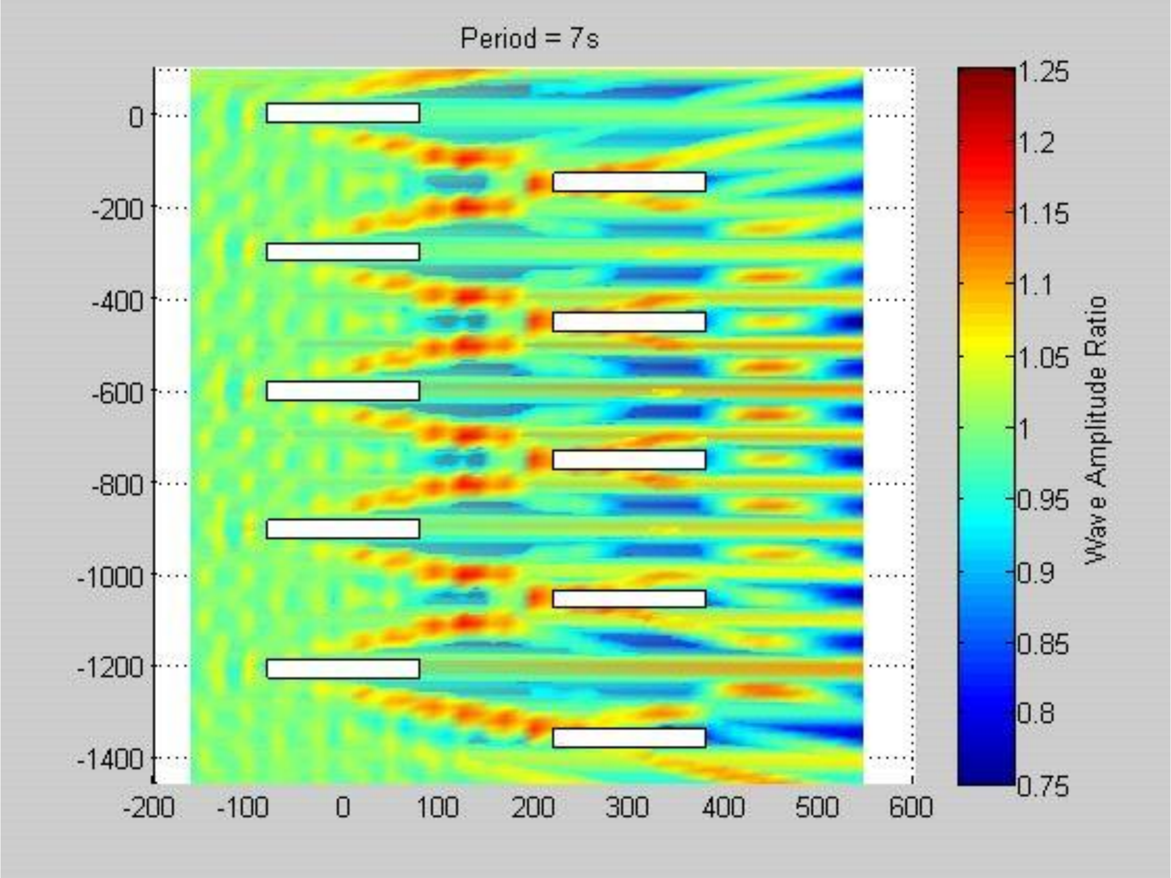

Figure 55: Wave Amplitude Ratio, 10 machines, 2LxL, T=7s

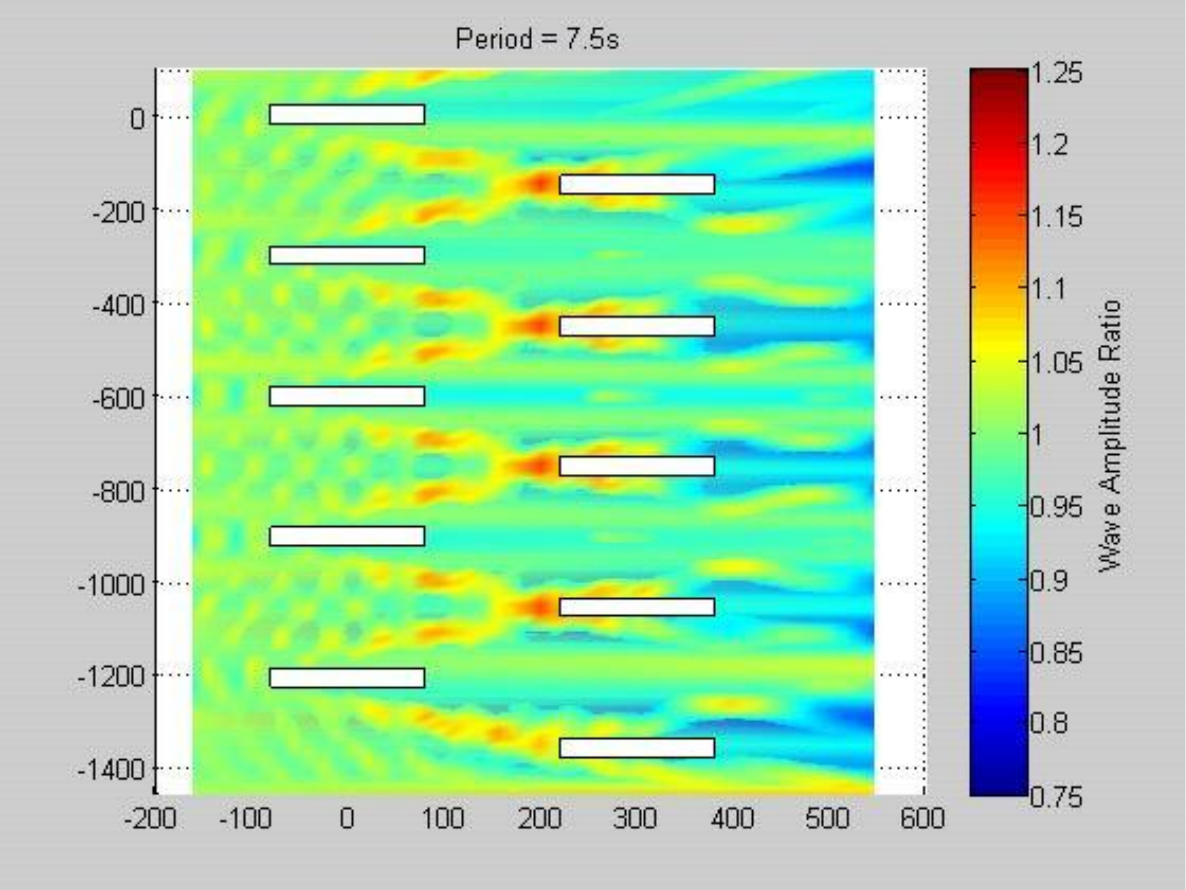

Figure 56: Wave Amplitude Ratio, 10 machines, 2LxL, T=7.5s

Shown in Figure 55 andFigure 56 is the wave field of a 10 machine set up at the optimal spacing of 2L x L for 7s and 7.5s period waves. Again, the wave heading is from the left, with the spacing of the machines shown in meters on the x and y axis. The amplification can be seen with wave amplitude ratios larger than 1 between the two rows.

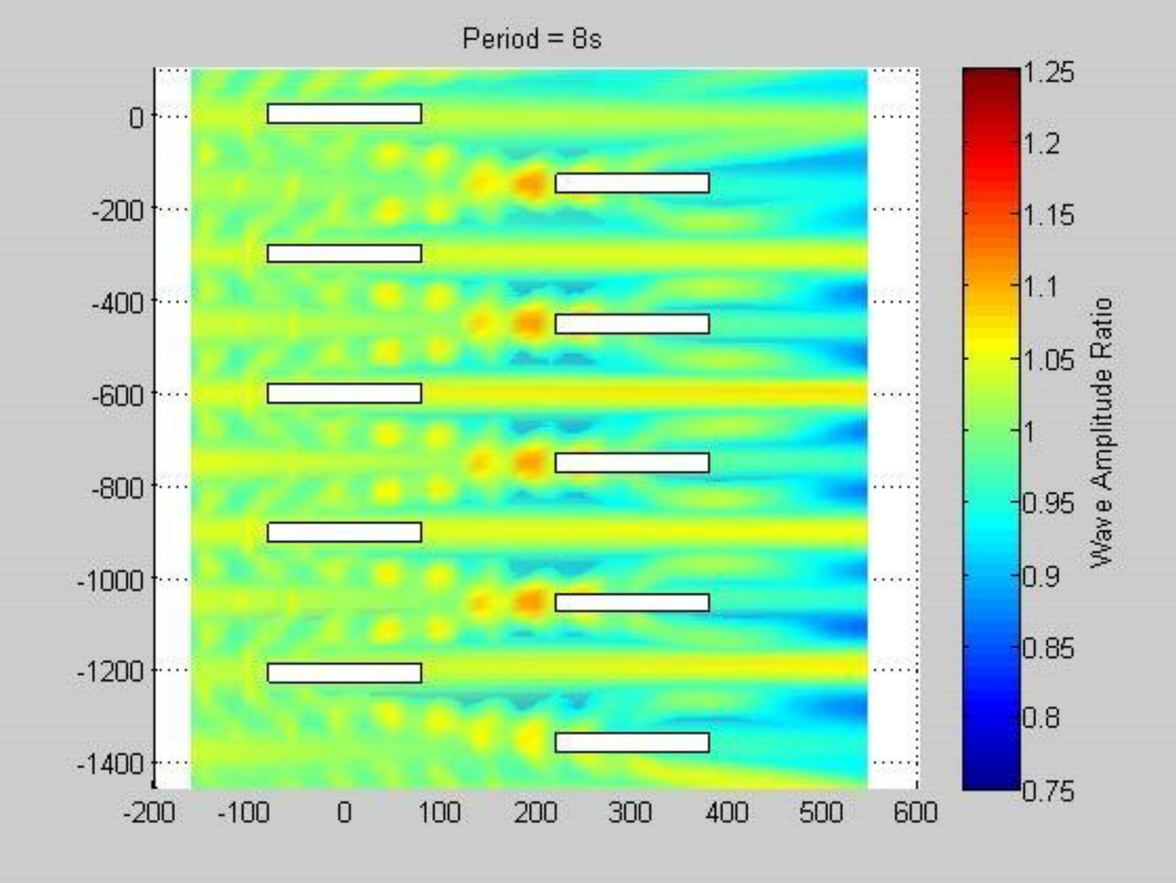

Figure 57: Wave Amplitude Ratio, 10 machines, 2LxL, T=8s

In Figure 57, the wave amplitude ratio is shown again for a wave period of 8s. The amplification and concentration of the wave energy is clearly visible with wave amplitude ratios of 1.2 and higher. These two periods were chosen due to large hinge motion, as shown in Figure 50, 51 andFigure 52.

11. Conclusion

Looking at the constructive amplification spacing on multiple machines shows an ideal scenario that may be practical. Due to environmental regulations and permitting, the area of the wave farm would need to be as small as possible while still retaining a good power factor Q. 10 machines at this spacing would cover an area of 675,000 m^2 rated at 7.5 MW. Using optimal sea states in the stormy North Atlantic[10], this would yield an output of 5.885 MW with a capacity factor of 78.4%, as seen in Figure 58.

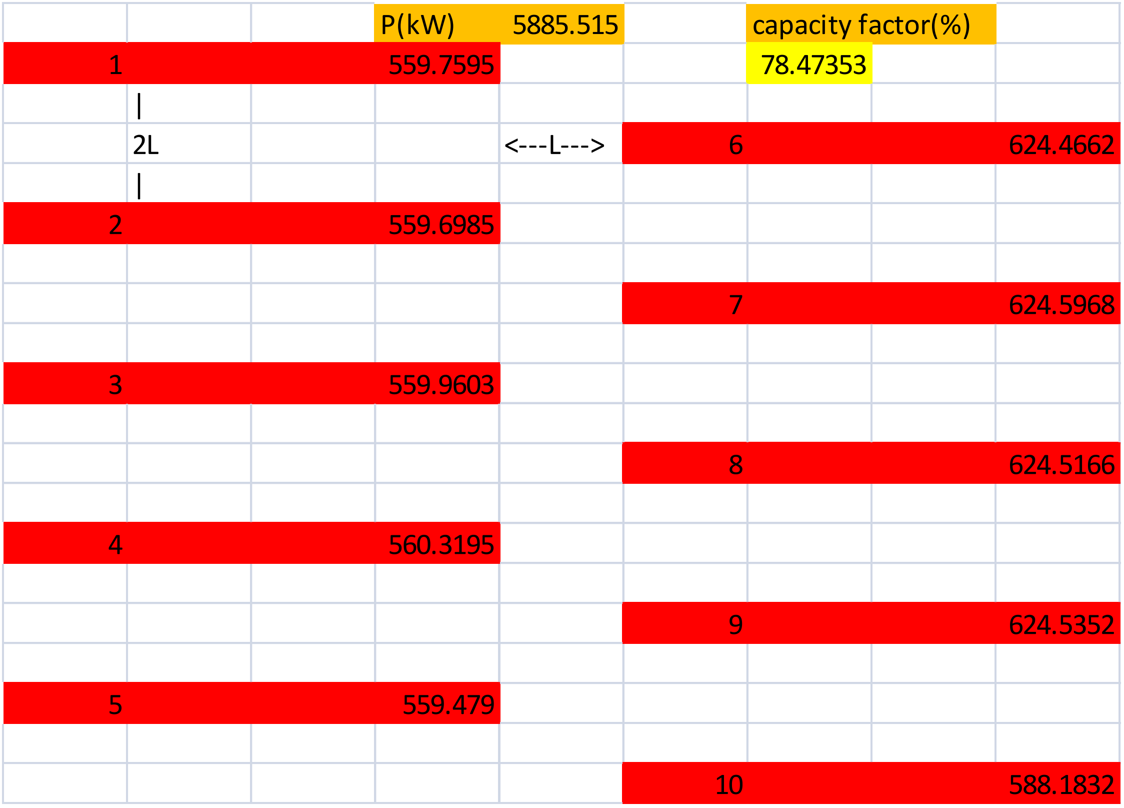

			P(kW)	5885.515		capacity factor(%)		
1			559.7595			78.47353		
	|							
	2L			<---L--->	6			624.4662
	|							
2			559.6985					
					7			624.5968
3			559.9603					
					8			624.5166
4			560.3195					
					9			624.5352
5			559.479					
					10			588.1832

Figure 58: Power Output of 10 Machines (2L x L) in North Atlantic Optimal Conditions - Losses Assumed

This would be an extremely good and unrealistic value for a coastal city in the Hawaiian Islands. Applying this 10 machine set up to spectral conditions for a location off of Oahu's windward shore at Kaneohe Bay gives a more realistic idea of power output for the Hawaiian Islands.

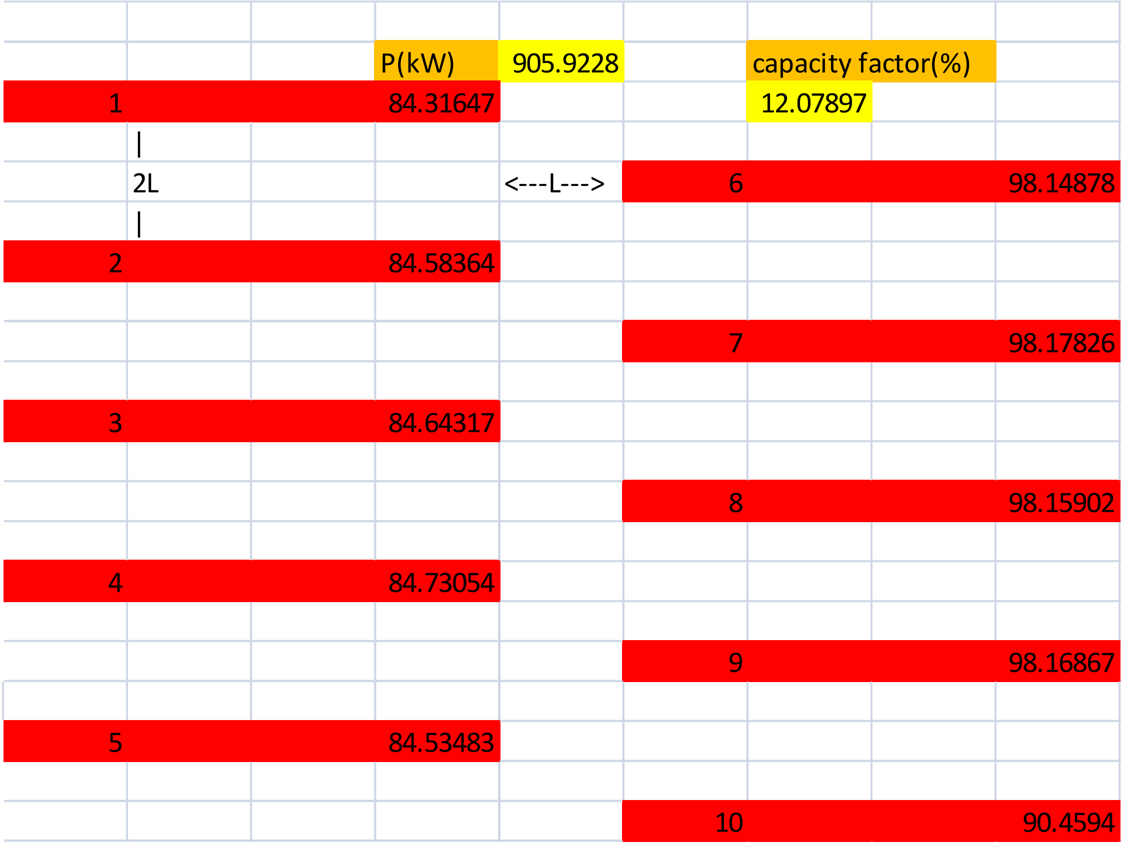

			P(kW)	905.9228		capacity factor(%)		
1			84.31647			12.07897		
	|							
	2L			<---L--->	6			98.14878
	|							
2			84.58364					
					7			98.17826
3			84.64317					
					8			98.15902
4			84.73054					
					9			98.16867
5			84.53483					
					10			90.4594

Figure 59: Power Output of 10 Machines (2L x L), Kaneohe, Hawaii - Losses Assumed

With a capacity factor of 12%, this output drop is not surprising as the State of Hawaii's wave resource is not of the same magnitude as the open waters of the North Atlantic. This would give an output of .905 MW for 675,000 m^2. Even with the optimal spacing, ideal conditions (direct heading) and no storage issues, this does not give a good energy density of 1.34 W/m^2. The L x .5L Pelamis® recommended spacing for 10 machines occupy an area of 281,250 m^2.

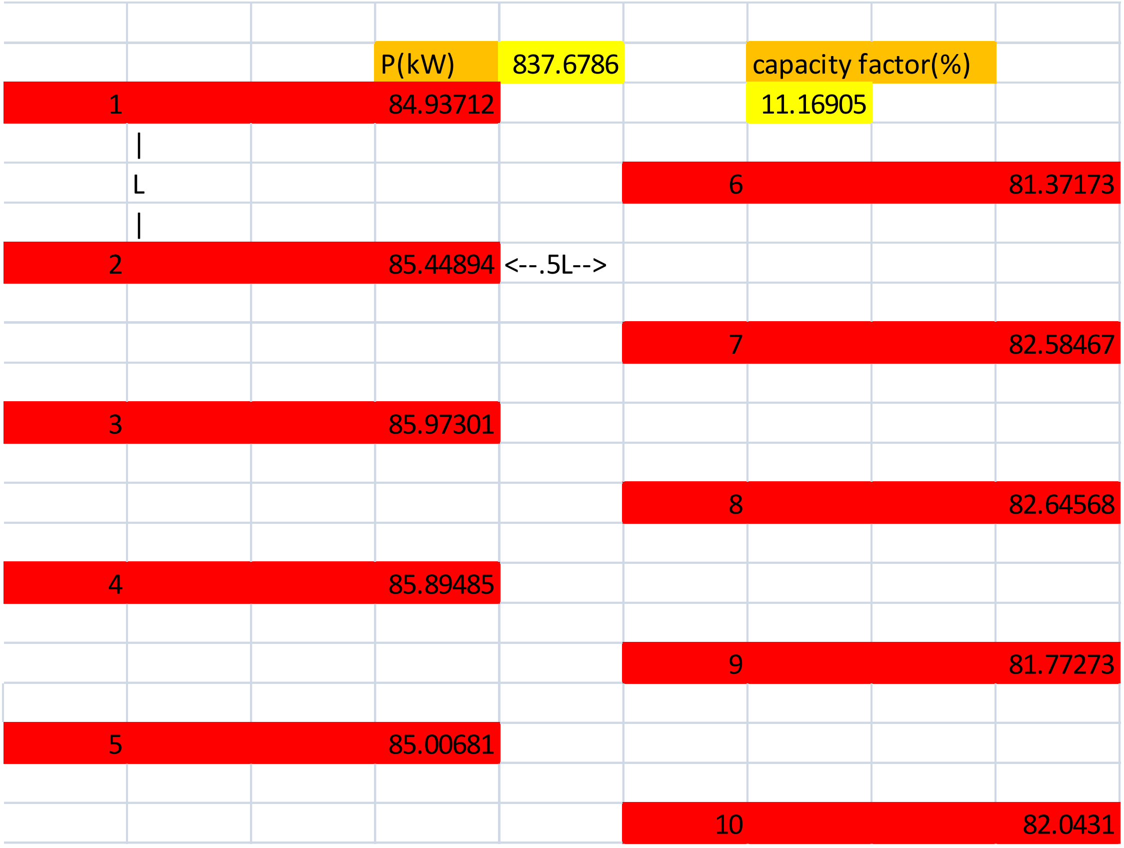

Figure 60: Power Output of 10 Machines (L x .5L), Kaneohe, Hawaii - Losses Assumed

This results in a smaller yearly average power output and capacity factor but a larger energy density of 2.97 W/m^2. While the optimal spacing of 2LxL only has a bit larger capacity factor, this addition in power due to constructive interference could be utilized for a large scale wave farm application. Assuming this gain is realistic, scaling it up would help a farm produce more power to make it competitive with other technologies. This phenomena should be utilized when implementing a large scale wave farm in order to get the most benefit from the number of machines. One could argue that this sort of analysis is necessary to maximize production in order to make it competitive and cost efficient.

12. Future Considerations

A next step in continuation of this study would be to add extra motions for the additional yaw hinge motions. For direct heading in this study, using only vertical hinge motions is sufficient, but for more realistic sea states with oblique seas, the horizontal motions of hinges also contribute to power production. In a real sea state, wave energy rarely comes from only one direction. Along with this, more in-depth runs will be needed for more accurate results for a large number of machines. This can be done using finer body meshes as well as more field points. In order to speed up this process, more CPUs can be used in a parallel architecture. A graphical user interface (GUI) can be created to simplify runs. This would entail an external code with a user friendly GUI that calls upon the WAMIT™ input files, and writes them according to specifics for each run. In doing this, it could also execute multiple runs, one after another. This would save “leg” work for the user.

References:

1. Haren, P. & Mei, C.C. "An Array of Hagen-Cockerell Wave Power Absorbers in Head Seas", J. Applied Ocean Research, 4(1):51-56 (1982).
2. WAMIT™ software; WAMIT™ Incorporated; Chestnut Hill, Massachusetts; www.wamit.com.
3. Pelamis® P-750 Wave Energy Converter, Pelamis® Wave power; Ocean Power Delivery Limited; Edinburgh, UK; www.pelamiswave.com.
4. Rhinoceros 5; McNeel North America; Seattle, Washington; www.rhino3d.com.
5. WAMIT™ User Manual Version 7.0; WAMIT™ incorporated; 2013; Chestnut Hill, Massachusetts; www.wamit.com.
6. Newman, J. N. *Marine Hydrodynamics*. MIT Press, 1977.
7. Newman, J. N. "Wave effects on deformable bodies", Applied Ocean Research, 16 (1994) 47-5.
8. Anast, Peter "Performance Trends of Hagen-Cockerell raft Wave Energy converters using WAMIT™ Software.", University of Hawaii at Manoa - Department of Ocean and Resources Engineering, January 2013.
9. Newman, Nick "Test24 - Hinge Damping Matrix." WAMIT™ Inc., 2012
10. International Association of classification Societies Ltd " Standard Wave Data", Nov. 2001; www.iacs.org.uk.
11. Cornett, Andrew M. "A Global Wave Energy Resource Assessment", International Offshore and Polar Engineering Conference, July 2008.
12. Newman, J.N. “Algorithms for the Free-Surface Green Function”, Journal of Engineering Mathematics, Vol. 19, pp. 57-67, 1985.
13. Nihous, Gerard “Wave Energy Lecture 10”[PowerPoint Slides], University of Hawaii, Ocean and Resources Department – ORE 677, Spring 2012.